Università degli Studi di Firenze

DOTTORATO DI RICERCA IN

"*Spettroscopia Atomica e molecolare*"

CICLO XXV

COORDINATORE Prof. Francesco Pavone

Mid Infrared digital holography and Terahertz imaging

Settore Scientifico Disciplinare FIS/01

Dottorando

Massimiliano Locatelli

Tutore

Dott. Paolo De Natale

Anni 2010/2012

Contents

Introduction

This PhD project was devoted to the development of imaging techniques in the Mid infrared and Terahertz regions. As we will see, these portions of the electromagnetic spectrum offer interesting and useful opportunities for imaging purposes under various points of view. In particular we focalized our attention toward the Mid infrared radiation generated by a high power CO_2 laser working at 10.6 μm and toward the 10 times longer far infrared radiation, at 111 μm, generated by a Quantum Cascade Laser. As we will see, each of these two long wavelength radiation sources has peculiar characteristics that can be fruitfully exploited for imaging. In this work, in particular, we decided to explore the possibilities offered by these sources in a specific imaging technique, Digital Holography. This is a quite recent technique (its birth dates back to 1994 by Schnars and Jüptner) and infrared radiation digital holography is still an almost unexplored research field. In particular, the first digital holography experiments at 10.6 μm were performed at the National Institute of Optics (INO), in Florence, about 10 years ago but only very recently, this technique has started receiving new attention because of its possible application to real time non-destructive testing of large size sample and to its possible involvement in the development of real 3d television. During this PhD project digital holography in the Mid infrared has been deeply investigated and innovative configurations and applications have been developed. Digital holography in the Terahertz region is an even more new development, the first results in this field being achieved very recently and under limitative conditions but, as every Terahertz imaging system, is rich in potential applications. During this PhD project we implemented a simple standard imaging technique in this spectral region and we used it to investigate the performances of a new kind of Terahertz radiation detectors: nanowire detectors. Finally, we traced the research lines we intend to develop in the field of Terahertz digital holography using QCL radiation.

The experiments presented in this work were obtained in the framework of a collaboration between the European Laboratory for Non Linear Spectroscopy (Lens), the CNR National Institute of Optics (INO-CNR), and the CNR Nanoscience Institute of Pisa (CNR-NANO), who provided the Terahertz source and the innovative detectors tested in this work.

In the **first chapter** we briefly review the basic principles of analog holography and describe, in more detail, its natural development, digital holography; in particular, in the last part of the chapter, we discuss the peculiar features that characterize digital holography with respect to the other imaging techniques. In the **second chapter** we introduce the basic notions about the two infrared regions object of our investigations and give a general description of some of the most interesting sources and detectors working in each of these two spectral ranges. We then focus on the possibility and opportunity to use infrared radiation to perform digital holography and discuss the advantages, and disadvantages, that this spectral region offers in this field. In the **third chapter** we describe and discuss the experimental apparatus and results obtained, during this PhD, in the field of infrared digital holography at 10.6 μm; in particular the paragraph about the experimental results is divided in five sections where different kind of experiments are illustrated in detail. In the **fourth chapter** we describe and discuss the experimental apparatus and results obtained, during this PhD, in the field of Terahertz imaging; in particular we illustrate the results obtained with a simple standard imaging setup and examine the possibility, and the opportunity, to translate the experimental configurations developed in the field of Mid infrared digital holography to the Terahertz range. In the **fifth chapter** we summarize the results obtained in the course of this PhD project and discuss their possible future developments and their potential applications.

1 Analog and digital holography

Holography was ideated in 1948 by the naturalized British Hungarian physicist Dénes Gábor, during his studies on the electronic microscope [18]. Gabor devised a technique to record and, subsequently, reconstruct both the amplitude and the phase information of a light wavefront diffracted by an object irradiated with coherent radiation; Gabor understood that this remarkable result could be obtained simply exploiting the interference pattern resulting from the superposition of the radiation coming from the object (*object beam*) with a portion of the radiation used for irradiating it (*reference beam*). Because of its ability to record the image of the object as a whole, the technique, initially called by Gabor simply 'Wavefront Reconstruction', acquired the name of 'Holography', from the Greek words 'holos', meaning whole, and 'graphein', meaning writing. The technique devised by Gabor was greeted initially with little interest by the scientific community, but starting by the '60s, that is when high spatial and temporal coherence radiation became easily accessible thanks to the invention of the laser, it underwent an important theoretical and experimental development so that Gábor, in 1971, was awarded the Nobel Prize in Physics for his invention.

In analog, or classical, holography, the interference pattern obtained by the superposition of the two beams is usually recorded on an analog image recording device (usually some appropriate kind of photographic film) that, once developed, constitutes the so-called 'hologram'; the object is then removed from its position and the transparency is repositioned at the point where it had been impressed; if the photographic plate is again irradiated by the reference beam, one observes the reconstruction, for diffraction, of a wavefront identical to the one coming from the object before it was removed; this means that the observer is invested by a light wavefront indistinguishable, with passive means, from the one generated by the object itself, and then, within a certain viewing angle, equipped with the same perspective and depth of focus.

Technological developments in computing and in image recording devices, have soon suggested the idea of transferring the analog recording and reconstruction processes of classical holography into the digital domain, giving rise to new techniques such as *Computer Generated Holography*, in which artificial interferograms of non-real objects, numerically created, are used to realize real holograms to be analogically reconstructed, and *Digital Holography*, in which the recording process is carried out by means of digital recording devices and the reconstruction process is performed numerically. The first step towards the realization of the latter technique was made in 1967 by Goodman and Lawrence [22] who managed to numerically reconstruct, in about 5 minutes, a digital hologram obtained from a real hologram recorded on a photographic film. The decisive step towards the complete digitalization of the holographic process was carried out in 1994 by Schnars and Jüptner [48] which realized, for the first time, the numerical reconstruction of a CCD recorded hologram. Thanks to technical progresses of modern CCD and CMOS devices and thanks to the higher computing power of today's computers, digital holography is experiencing massive growth and, because of its methodological simplicity, is replacing, in most applications, the corresponding classical technique; this process is further speeded up by the fact that the major manufacturers of the most popular photographic films used in analog holography have closed down their production lines due to the general tendency to prefer modern digital technologies. However, to date, this technique still suffers from some limitations due to the lower resolution of electronic recording devices compared to analog ones, limitations intended to diminish with the advent of bigger and bigger CCDs with increasing resolution. The long time required for the numerical reconstruction that, in the early days of this technique, constituted a significant limitation for the development of digital holography, have now been greatly reduced and modern calculators allow, in many cases, a reconstruction substantially simultaneous with the hologram recording procedure. Real time wavefront

reconstruction, made it possible by digital holography, represents today a very important and attractive tool in numerous applications.

1.1 Analog holography

As already mentioned in the previous section, the goal of holography is the recording and subsequent reconstruction of the amplitude and phase information of the wavefront coming from an object irradiated with coherent radiation; holography is therefore a two-step process, a first step to record the interference pattern, the hologram, and a second step to reconstruct the object wavefront or, as is usually said, to reconstruct the hologram.

1.1.1 Wavefront recording

Image recording devices provides a response proportional to the average energy impinging on their surface; their response is therefore proportional to the *irradiance*, or *average intensity*, I, of the electromagnetic field; this physical quantity, in fact, represents the average energy transported from the field, in the direction of propagation of the field itself, divided for the time and surface units; the average is performed on a time T_m much greater than the period of the electromagnetic wave and therefore the irradiance measurement results directly proportional to the square amplitude of the field but any information on its phase distribution is lost; for this reason, if the wavefront phase information is of interest too, it is necessary, somehow, to bring back the phase measurement to an irradiance measurement. The idea at the basis of holography is precisely to exploit the phenomenon of interference between electromagnetic waves to incorporate the phase information in the intensity information. In holography, in particular, the phase information of the object wavefront is 'written' in the interference pattern created by the object beam and an appropriate reference beam.

Depending on the nature of the object under investigation two different holographic configurations, with respect to the origin of the object beam, are possible: transmission holographic configuration and reflection holographic configuration.

For **transparent samples** the coherent radiation passes through the sample so that the ballistic radiation transmitted through the object itself, modified by its transparency characteristics, constitutes the object beam (figure 1.1).

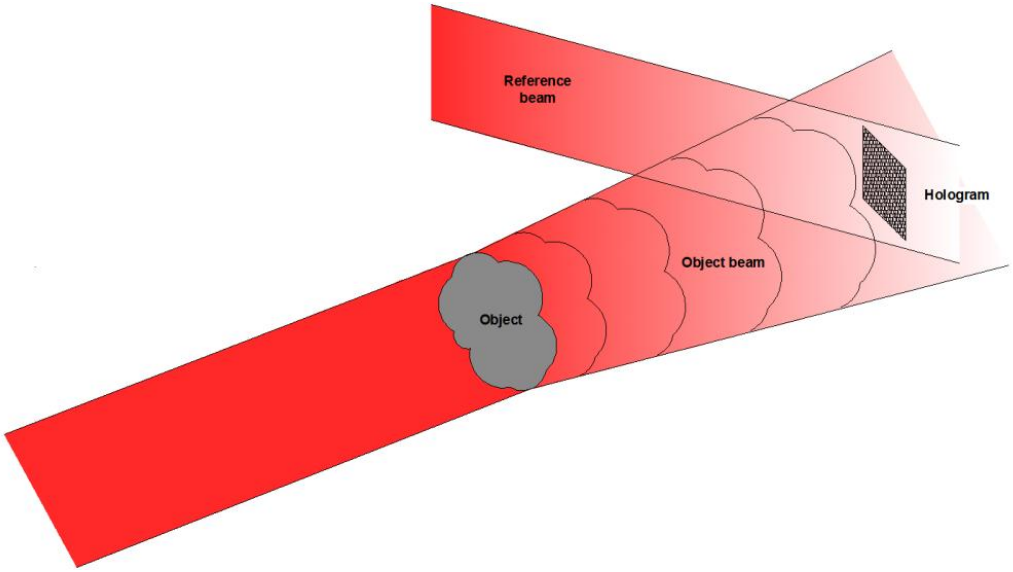

Figure 1.1: General transmission holographic configuration.

In this case, both the local absorption coefficient of the material which constitutes the sample and the optical path that the beam travels within the sample itself, affect the wavefront emerging from the sample; in the first case, the beam undergoes a change in its amplitude while, in the second case, it undergoes a phase change depending on the local refractive index of the material and on the local thickness of the sample.

For **opaque samples** the coherent radiation is directed toward the sample so that the reflected, or scattered, radiation in the direction of the recording device constitutes the object beam (figure 1.2).

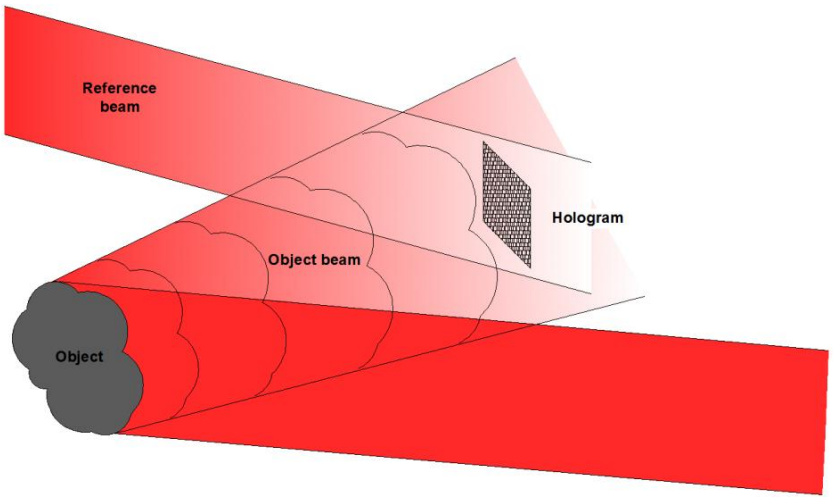

Figure 1.2: General reflection holographic configuration.

In the ideal case of a totally reflecting object (that is with surface roughness much shorter than the wavelength in use) the recording device receives only the radiation directly reflected from the object according to the laws of geometrical reflection; in this case it is possible to record in the hologram only the information of that portion of the object wavefront directly reflected toward the recording surface. If instead the surface of the object presents a roughness comparable to the wavelength in use, one can think the object as consisting of a huge number of small reflective elements with random orientation each of which irradiate in a different direction and one speaks, in that case, of scattered radiation; the various waves emitted by these microscopic sources interfere with each other and what is observed on the recording surface is a dotted image composed of a set of bright and non-luminous randomly distributed small spots, the so called *speckles* [47]; in principle, any portion of the recording device can thus collect the information coming from each portion of the object, regardless of its size; in this configuration, called *speckle holography*, therefore, it is possible to use any portion, however small, of the hologram, to reconstruct the entire wavefront, even though, as we will see, the smaller the portion of the hologram, the lower will be the final reconstruction resolution. We have to consider also that, in holography, speckles contain the information on the desired object wave but reduce,

at the same time, the final reconstruction resolution; in particular, the effect of this noise is linked to the size of the speckles observed in the reconstructed image plane, namely the so-called *subjective speckles*, so that the larger the speckles the more disturbing they are. It can be shown that a larger subjective speckle size is obtained by reducing the hologram aperture [47]. Real objects never act as ideal reflectors and thus, in practice, one can always think of being in a case, more or less marked, of scattering object; what changes is just the percentage of scattered radiation that ends up in the recording device.

The object beam and the reference beam usually travel different paths but, in order to obtain interference fringes, they must be coherent with each other and therefore, usually, are extracted from a single laser beam by means of suitable beam splitters. For the same reason, the two paths must be equal within a value lower than the laser coherence length. Furthermore, as in every interferometry experiment, in order to get good interference fringe visibility, the two beams should have comparable intensity and the differences between the two optical paths should be kept stable, within a fraction of the wavelength, during the time required to perform the hologram recording. Finally, as we will see later, in order to obtain an undistorted reconstructed object wavefront during the reconstruction step, the reference beam amplitude has to be uniform across the recording device surface; strictly speaking every homogeneous reference wave could therefore be used; usually, however, only plane waves or large curvature spherical waves are employed.

If we consider monochromatic waves of frequency ω and if we denote with $\mathcal{E}_o(x,y) = E_o(x,y)e^{i\phi_o(x,y)}$ and $\mathcal{E}_r(x,y) = E_r e^{i\phi_r(x,y)}$ the complex amplitudes of the object and reference beam respectively on the generic plane (X,Y), the total irradiance of their interference field on the recording plane, or hologram plane, (X_H, Y_H), is

$$I(x_H, y_H) \propto |\mathcal{E}_o(x_H, y_H) + \mathcal{E}_r(x_H, y_H)|^2 =$$

$$= |\mathcal{E}_o(x_H, y_H)|^2 + |\mathcal{E}_r(x_H, y_H)|^2 + \mathcal{E}_o^*(x_H, y_H)\,\mathcal{E}_r(x_H, y_H) + \mathcal{E}_o(x_H, y_H)\,\mathcal{E}_r^*(x_H, y_H) =$$
$$= E_o^2(x_H, y_H) + E_r^2 + 2E_o(x_H, y_H)E_r \cos[\phi_r(x_H, y_H) - \phi_o(x_H, y_H)]$$

The first two terms of this last expression depend only on the amplitude of the two fields, the third term, instead, depends directly on their relative phase; the interference pattern recorded on the hologram results thus to be a function of both the amplitude and the phase of the object field. The recording medium, whatever it is (silver halide photographic slab, photorefractive material, photopolymer, dichromatic jelly, etc.), must be used within the linearity region of its transmittance vs exposure curve and provides, in this case, a linear mapping of the resulting field intensity, in the sense that, once developed, locally changes its physical characteristics (absorption coefficient, refractive index, thickness, ...) so as to present a transparency $H(x_H, y_H)$ linearly proportional to the incident irradiance

$$H(x_H, y_H) = h_0 + \beta\tau I(x_H, y_H) =$$
$$= h_0 + \beta\tau[|\mathcal{E}_o(x_H, y_H)|^2 + |\mathcal{E}_r(x_H, y_H)|^2 + \mathcal{E}_o^*(x_H, y_H)\,\mathcal{E}_r(x_H, y_H)$$
$$+ \mathcal{E}_o(x_H, y_H)\,\mathcal{E}_r^*(x_H, y_H)]$$

where

h_0 is the transparency of the unexposed plate (not present in digital holography)

τ is the exposure time

β is a proportionality constant characteristic of the recording medium (negative for photographic emulsions).

1.1.2 Wavefront reconstruction

The second step in a holography experiment is the reconstruction of the object wavefront 'recorded' in the hologram. Once the holographic plate is chemically developed it is rearranged in its original position while the object is removed; at this point the plate can be considered as a diaphragm equipped with the transparency, or

transmittance (in general complex), calculated above. The holographic reconstruction is then obtained by sending an appropriate beam, the so-called *reconstruction beam*, in order to create, for diffraction through the hologram, a wavefront identical to the one previously coming from the object.
If we send on the transparency a generic reconstruction beam $\mathcal{R}(x,y)$, the expression of the wave at the exit of the transparency is

$$\mathcal{E}(x_H,y_H) = \mathcal{R}(x_H,y_H)\,H(x_H,y_H) =$$
$$= \mathcal{R}(x_H,y_H)h_0 + \mathcal{R}(x_H,y_H)\beta\tau|\mathcal{E}_o(x_H,y_H)|^2 + \mathcal{R}(x_H,y_H)\beta\tau|\mathcal{E}_r(x_H,y_H)|^2 +$$
$$+ \mathcal{R}(x_H,y_H)\beta\tau\mathcal{E}_o^*(x_H,y_H)\mathcal{E}_r(x_H,y_H) + \mathcal{R}(x_H,y_H)\beta\tau\mathcal{E}_o(x_H,y_H)\mathcal{E}_r^*(x_H,y_H)$$

If we use, as a reconstruction beam, a beam exactly identical to the one used to record the hologram, namely $\mathcal{R}(x,y) = \mathcal{E}_r(x,y)$, the wavefront at the exit of the hologram becomes

$$\mathcal{E}(x_H,y_H) =$$
$$= \mathcal{E}_r(x_H,y_H)h_0 + \mathcal{E}_r(x_H,y_H)\beta\tau|\mathcal{E}_o(x_H,y_H)|^2 + \mathcal{E}_r(x_H,y_H)\beta\tau|\mathcal{E}_r(x_H,y_H)|^2 +$$
$$+ \mathcal{E}_r(x_H,y_H)\beta\tau\mathcal{E}_o^*(x_H,y_H)\mathcal{E}_r(x_H,y_H) + \mathcal{E}_r(x_H,y_H)\beta\tau\mathcal{E}_o(x_H,y_H)\mathcal{E}_r^*(x_H,y_H) =$$
$$= \left\{\left[h_0 + \beta\tau[E_o^2(x_H,y_H) + E_r^2]\right]\right\}\mathcal{E}_r(x_H,y_H) + \beta\tau\mathcal{E}_r^2(x_H,y_H)\mathcal{E}_o^*(x_H,y_H)$$
$$+\beta\tau E_r^2\mathcal{E}_o(x_H,y_H)$$

This equality in the plane of the hologram is valid, thanks to the principle of existence and uniqueness of differential equation with fixed contour condition (on the hologram plane output), in every plane (X,Y) of the observation half-space and we can therefore write, more generally

$$\mathcal{E}(x,y) = \{h_0 + \beta\tau[E_o^2(x,y) + E_r^2]\}\mathcal{E}_r(x,y) + \beta\tau\mathcal{E}_r^2(x,y)\mathcal{E}_o^*(x,y) + \beta\tau E_r^2\mathcal{E}_o(x,y)$$

The first term of this expression is the so-called *undiffracted* (or *zero-order* or *DC*) term and coincides with the reconstruction (and reference) beam $\mathcal{E}_r(x,y)$ except for

a multiplicative factor in general dependent on the spatial variables. The interpretation of the second term is a bit more complex but it can be shown [47;21], by means of the so-called *imaging equations*, that it converges to form a real pseudoscopic and distorted object image, placed, with respect to the hologram plane, in the half-space opposite to the one where the object was situated originally; this image is distorted because of the complex factor, depending on the space variables, $\mathcal{E}_r^2(x,y)$. The third term coincides with the object beam $\mathcal{E}_o(x,y)$ except for a real multiplication factor which influences exclusively, locally, its brightness; this term is just what we needed, namely a wavefront identical, except for a uniform multiplication factor, to the one coming from the object during the recording process; an observer positioned in the half-space opposite to the object original position with respect to the hologram plane, can thus see a virtual image, originating beyond the hologram, substantially identical to what he perceived in the presence of the 'real object', completely indistinguishable, apart from a possible brightness uniform attenuation, from the original one.

If an undistorted real image of the object is desired, it is possible to illuminate the hologram with a reconstruction beam equal to the complex conjugate of the reference beam, $\mathcal{R}(x,y) = \mathcal{E}_r^*(x,y)$, in which case we have

$$\mathcal{E}(x_H, y_H) =$$
$$= [h_0 + \beta\tau(E_o^2 + E_r^2)]\mathcal{E}_r^*(x_H, y_H) + \beta\tau E_r^2 \mathcal{E}_o^*(x_H, y_H) + \beta\tau \mathcal{E}_r^{*2}(x_H, y_H)\, \mathcal{E}_o(x_H, y_H)$$

Here the undistorted term is just the one relative to $\mathcal{E}_o^*(x_H, y_H)$ which, as we have said, produces the real image of the object under examination.

1.1.3 On-axis and off-axis holography

In the configuration originally designed by Gabor, subsequently defined on-axis holography, the object and the reference beams were both coaxial with the axis of the recording plate; in particular, in the experiment by Gabor, the object was a highly

transparent object with weak transmittance variations with respect to the medium transmittance; in these conditions both the reference and the object beam could be directly obtained from the same laser beam which, passing through the sample, was split into two parts: a major portion of the beam which continued undisturbed and worked as a reference beam and a minor portion of it which was diffracted by the transmittance changes of the sample and which constituted the object beam. This kind of configuration, however, presents a problem, the so-called *twin image problem*: the three diffraction orders forming the reconstructed wavefront (the real image, the virtual image and the undiffracted order) are spatially superimposed in the observation direction, troubling each other. To overcome this drawback, in 1962 Leith and Upatnieks devised what was defined *off-axis configuration* [31]; in this configuration the reference beam and the object beam are not coaxial with the axis of the recording plane but are inclined to each other by an angle θ; with the increasing of this angle the interference fringes frequency increases rapidly until fringes become indistinguishable to the naked eye, and, as we shall see, in the hologram reconstruction, the real image, the virtual image and the zero order term spatially separate progressively in proportion to this inclination angle. Assuming that the object is positioned in front of the recording plate so that the object beam is mainly directed along the hologram axis (Z axis) and assuming that the reference beam is a plane wave inclined with respect to the hologram plane by an angle θ along the Y axis, $\left(\vec{k} = k \sin\theta\, \hat{y} + k \cos\theta\, \hat{z}\right)$, we can write, on the hologram plane ($z = 0$),

$$\mathcal{E}_r(x, y) = E_r e^{i2\pi\alpha y}$$

with $\alpha = \frac{\sin(\theta)}{\lambda}$

The intensity pattern resulting from the interference of the two beams on the hologram plane is therefore

$$I(x_H, y_H) = |\mathcal{E}_o(x_H, y_H)|^2 + \left|E_r e^{i2\pi\alpha y}\right|^2 + \mathcal{E}_o^*(x_H, y_H)E_r e^{i2\pi\alpha y} + \mathcal{E}_o(x_H, y_H)E_r e^{-i2\pi\alpha y} =$$
$$= E_o^2(x_H, y_H) + E_r^2 + 2E_o(x_H, y_H)E_r \cos[2\pi\alpha y - \phi_o(x_H, y_H)]$$

This expression shows that the amplitude and the phase of the wavefront coming from the object are recorded, respectively, as amplitude and phase modulations of a carrier frequency α and, as we shall see, if the carrier frequency is sufficiently high, the amplitude and phase distributions can be recovered without any orders superposition from the interference pattern.

If we perform the hologram reconstruction by means of a plane reconstruction wavefront normal to the hologram plane and with the same amplitude of the plane reference beam, we obtain

$$\mathcal{E}(x, y) =$$
$$= \{h_0 + \beta\tau[E_o^2(x, y) + E_r^2]\}E_r + \beta\tau E_r^2 e^{i2\pi\alpha y}\mathcal{E}_o^*(x, y) + \beta\tau E_r^2\, e^{-i2\pi\alpha y}\mathcal{E}_o(x, y) =$$
$$= (h_0 + \beta\tau E_r^2)E_r + (h_0 + \beta\tau E_r^2)E_o^2(x, y)E_r$$
$$+\beta\tau E_r^2 e^{i2\pi\alpha y}\mathcal{E}_o^*(x, y) + \beta\tau E_r^2 e^{-i2\pi\alpha y}\,\mathcal{E}_o(x, y)$$

The first term of the last expression is simply an attenuated version of the reconstruction beam and then, like this one, it propagates in the direction normal to the plane of the hologram, i.e. in the direction of the observer. The second term instead, while being proportional to the reconstruction beam, due to the spatial dependence of the coefficient $E_o^2(x, y)$, is composed of plane waves traveling at different angles with respect to the reconstruction beam propagation direction; however, if the frequencies of $E_o^2(x, y)$ are sufficiently small compared to the frequency of the carrier α, the energy of this term remains sufficiently close to the main propagation direction. The third term, the one giving rise to the real image of the object, is deflected by an angle $-\theta$ with respect to the Z axis. Finally, the fourth term, the one giving rise to the object virtual image, is deflected by an angle $+\theta$ with

respect to the Z axis. Thanks to this stratagem the beams are thus shifted each other and, for sufficiently high θ angles their overlapping is avoided, as shown in figure 1.3.

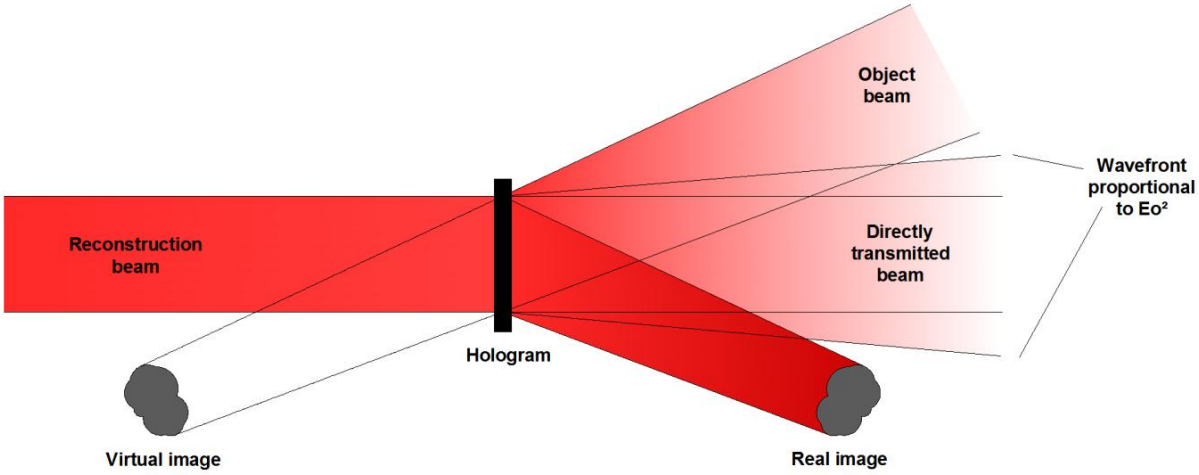

Figure 1.3: Off axis holographic configuration.

A completely analogous result can be obtained using spherical reference and reconstruction beams with sufficiently large curvature radii and different curvature centres positions [21]. If the distance between the recording plane and the origin of the reference spherical wave is equal to the distance between the recording plane and the object position, we obtain a remarkable holographic configuration called *lensless Fourier holography* with peculiar properties.

To estimate the value of the minimum angle at which we must operate in order to separate real image, virtual image and undiffracted term, it is sufficient to determine the minimum value of the carrier wave frequency for which the various spectral terms do not overlap. In particular it is possible to demonstrate [21] that the three orders separation condition is fulfilled if the following inequality is satisfied

$$\theta \geq \sin^{-1} 3B\lambda$$

Where B is the higher spatial frequency of the object wavefront.
If the reference wave is much stronger than the object beam the zero order term can be ignored and the previous inequality reduces to [21]

$$\theta \geq \sin^{-1} B\lambda$$

In analog holography, where very high resolution recording devices are used and very narrow fringes are therefore recordable, it is possible to tilt the reference beam up to very high θ values and it is thus always possible to separate the three components of the reconstructed wavefront. It is then possible to cut the undesired contributions by means of an appropriate spatial filter on the focal plane of a suitable converging lens placed in front of the transparency, that is on the plane where it materializes the Fourier transform of the signal; after selecting the contribution of interest it is then possible to reconstruct the relative wavefront anti transforming the signal with a second identical lens.

1.2 Digital holography

From the point of view of the theory and the purposes, Digital Holography (DH) is directly derived from analog holography but differs from the classical technique for the hologram recording medium and for the wavefront reconstruction method. While, in fact, in classical holography the interferogram recording process is performed by means of appropriate photosensitive materials which need to be developed before being used in the reconstruction process, in DH the recording medium is, more simply, a digital device, typically a CCD or a CMOS device. The interference pattern containing the information about the wavefront to be studied is thus sampled and digitized by the electronics of the device and stored in the memory of a computer. The reconstruction of the wavefront, obviously, can no longer be carried out in an optical way, at least not directly, but it is performed numerically by means of appropriate

algorithms through standard calculation software; it is thus possible to derive the desired information on the wavefront under investigation, amplitude and phase, and to reconstruct the wavefront in a digital version too.

1.2.1 Wavefront recording

As we have just said, the recording process in DH is greatly simplified with respect to classical holography; analog photographic plates and complicated development techniques are no longer required but all it is needed is a detector working with the radiation in use and an image processing program to record the interference pattern. Current electronic recording devices, however, have a much smaller spatial resolution with respect to old photographic plates: the resolution attainable with a classic support can reach up to a maximum of about $7000 cycles/mm$ (where cycle means a pair of white/black fringes) while a CCD with square pixels of lateral dimensions greater than $5\mu m$ (a typical values in CCD cameras) allows to solve a maximum of $100 cycles/mm$. This limitation is particularly restrictive when working in off-axis holography where the maximum recordable number of $cycles/mm$ directly imposes a limit on the angle θ between the reference beam and the normal to the sensor. If we refer, in particular, to speckle holography, in optimal recording conditions, the recording device should be able to solve entirely the interference pattern resulting from the superposition of the reference wave with all the waves spread by all the different points constituting the object under investigation. The maximum value of the angle θ is thus related to the lateral dimension of the object, to the lateral dimension of the detector and to the distance between them. If, for simplicity, we refer to the simplified one-dimensional configuration sketched in figure 1.4, we can quantify these relations by means of simple geometrical considerations.

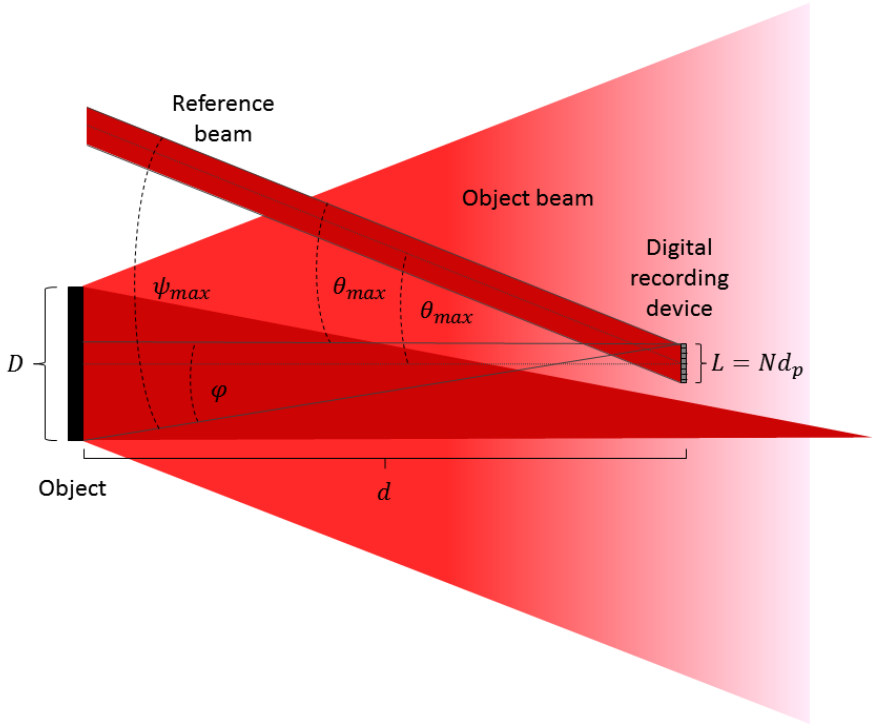

Figure 1.4: Maximum θ angle value according to the sampling condition.

If we want that all the object point sources contribute to the interference pattern across the entire detector, it is necessary that the interference fringes between the reference beam and the highest spatial frequency component of the object wave can be recorded by the detector; if we indicate with φ the angle formed by the highest spatial frequency originating in the object with respect to the detector axis, we observe [47], across the sensor, a sinusoidal interference fringe pattern between this highest spatial frequency and the reference beam with period

$$P = \frac{\lambda}{\sin\theta + \sin\varphi} = \frac{\lambda}{2\sin\left(\frac{\theta+\varphi}{2}\right)\cos\left(\frac{\theta-\varphi}{2}\right)}$$

Which, for $\theta \cong \varphi$ and $\theta + \varphi = \psi$, becomes

$$P \cong \frac{\lambda}{2\sin\left(\frac{\psi}{2}\right)}$$

The maximum angle ψ_{max} allowed by Whittaker-Shannon sampling theorem is reached when the value of the fringe period reaches its minimum admitted value P_{min} equal to two times the detector pixels lateral dimension d_p

$$P_{min} = \frac{\lambda}{2\sin\frac{\psi_{max}}{2}} = 2d_p$$

the maximum angle ψ_{max} results thus to be

$$\psi_{max} = 2\sin^{-1}\left(\frac{\lambda}{4d_p}\right)$$

For small ψ angle values, it is possible to approximate the sin function with its argument, obtaining

$$\psi_{max} \overset{small\ angle}{\approx} \frac{\lambda}{2d_p}$$

Considered the typical pixel pitch values at each wavelenght, it follows, from the last equation, that the small angle approximation is usually well satisfied.
With simple geometric considerations it is thus simple to calculate the maximum value θ_{max}, that is

$$\theta_{max} = \psi_{max} - \varphi = 2\sin^{-1}\left(\frac{\lambda}{4d_p}\right) - \tan^{-1}\left(\frac{\frac{D}{2}+\frac{L}{2}}{d}\right) \overset{small\ angles}{\approx} \frac{\lambda}{2d_p} - \frac{D+L}{2d}$$

Where

D is the object lateral dimension,

L is the sensor lateral dimension,

d is the object-sensor distance

If the object lateral dimension is much larger than the lateral sensor dimension the previous expression simplifies further and becomes

$$\theta_{max} = \frac{\lambda}{2d_p} - \frac{D}{2d} = \frac{d\lambda - d_p D}{2dd_p}$$

This limitation on the angle θ, may lead, during the reconstruction process, to a partial overlapping of the three diffraction orders or, in other words, if the object dimensions are fixed, imposes a limit on the minimum distance between the object and the sensor: when the distance d is reduced the angle φ increases and, consequently, the maximum admitted value of θ decreases and may exceed the minimum value admitted to ensure the orders separation.

As we will see, in digital holography, the zero order term can be removed, during the reconstruction process, by means of various numerical algorithms and therefore, in order to separate the real and the virtual image, it is sufficient that the angle θ satisfies the less restrictive inequality

$$\theta \geq \theta_{min} = \sin^{-1} B\lambda$$

If we refer to the simplified configuration of figure 1.5, it follows that, for a fixed value of lateral object dimension and for a certain distance between the object and the recording device, the angle θ can't be smaller than the angle φ between the highest spatial frequency wave originating in the object and the normal to the sensor; in other

terms, the minimum angle condition is obtained when the reference beam passes just adjacent to the object.

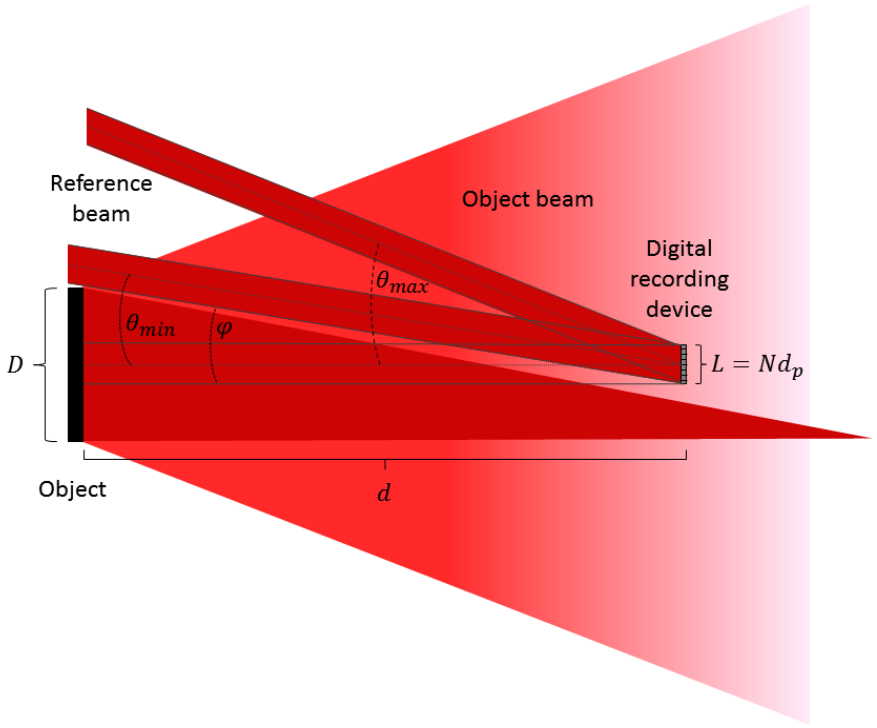

Figure 1.5: Minimum θ angle value to have the three orders separation.

1.2.2 Wavefront reconstruction

As we have already mentioned, the wavefront reconstruction in digital holography is performed numerically by means of mathematical algorithms derived from the diffraction theory.

If we consider the hologram as an optical transmittance positioned on the recording plane (X_H, Y_H), the reconstructed wavefront at a distance d, in the reconstruction plane (X_R, Y_R), is in fact the result of the diffraction operated on the reconstruction beam by the hologram window (figure 1.6).

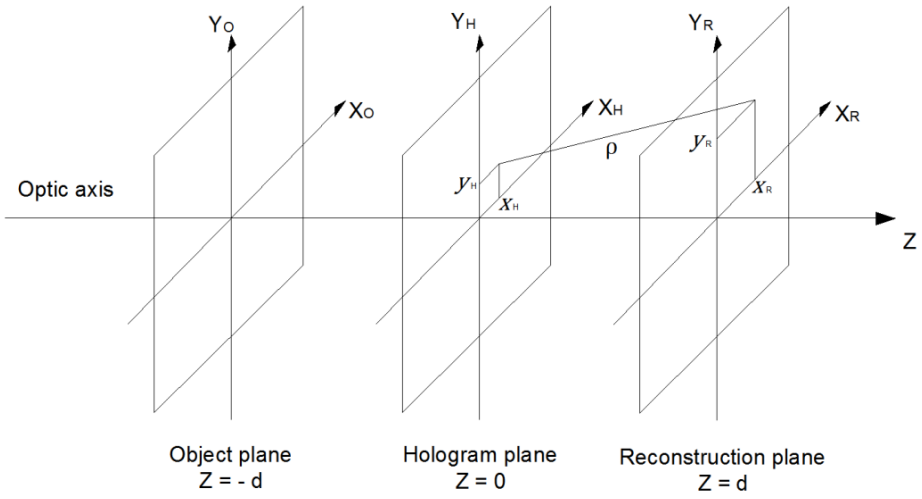

Figure 1.6: Object plane, hologram plane and reconstruction plane.

To obtain numerically the analytical expression of such a wavefront we can exploit the Rayleigh-Sommerfeld formula [5] that, by placing the obliquity factor equal to 1 [47], is written in this case

$$\mathcal{E}(x_R, y_R) = \frac{1}{i\lambda} \iint_{-\infty}^{+\infty} \mathcal{R}(x_H, y_H) H(x_H, y_H) \frac{e^{i\frac{2\pi}{\lambda}\rho}}{\rho} \, dx_H dy_H$$

where

$\lambda =$ wavelength used to reconstruct the hologram,

$H(x_H, y_H) =$ intensity of the interferogram in the hologram plane,

$\mathcal{R}(x_H, y_H) =$ wavefront reconstruction beam in the hologram plane,

$\rho = \sqrt{d^2 + (x_R - x_H)^2 + (y_R - y_H)^2} =$ distance between the generic point of the recording plane (X_H, Y_H) and the generic point of the reconstruction plane (X_R, Y_R),

$d =$ distance between the recording plane (X_H, Y_H) and the reconstruction plane (X_R, Y_R).

Once obtained the numerical expression of the complex reconstructed wavefront $\mathcal{E}(x_R, y_R)$, it is possible to extract from it the intensity value $I(x_R, y_R)$ and the phase value $\phi(x_R, y_R)$ of the object wavefront in the reconstruction plane

$$I(x_R, y_R) = \mathcal{E}(x_R, y_R)\, \mathcal{E}^*(x_R, y_R) \quad , \quad \phi(x_R, y_R) = \tan^{-1}\left(\frac{Im\{\mathcal{E}(x_R, y_R)\}}{Re\{\mathcal{E}(x_R, y_R)\}}\right)$$

where $Re\{\mathcal{E}(x_R, y_R)\}$ and $Im\{\mathcal{E}(x_R, y_R)\}$ denote, respectively, the real part and the imaginary part of the complex amplitude $\mathcal{E}(x_R, y_R)$.

The double integration of the Rayleigh-Sommerfeld formula involves considerable calculating effort but fortunately we will see that, in order to simplify its numerical implementation, it is possible to convert this integral in one or more two-dimensional Fourier transforms; considered that, in case of digital recording, the complex function $H(x_H, y_H)$ in the hologram plane is discretized, the previous transforms are actually discrete Fourier transforms, more easily calculable by means of existing Fast Fourier Transform (FFT) algorithms. To operate this transformation there are two methods, the *Fresnel method* and the *convolution method*.

Fresnel Method

For values of x_R, y_R, x_H, y_H small compared to the distance d between the reconstruction plane and the hologram plane, the expression of $\rho = \sqrt{d^2 + (x_R - x_H)^2 + (y_R - y_H)^2}$ can be approximated with its Taylor development

$$\rho \approx d + \frac{(x_R - x_H)^2}{2d} + \frac{(y_R - y_H)^2}{2d} - \frac{[(x_R - x_H)^2 + (y_R - y_H)^2]^2}{8d^3} + \cdots$$

The fourth term of this expression can be neglected if it is small compared to the wavelength [21], i.e. if

$$\frac{[(x_R - x_H)^2 + (y_R - y_H)^2]^2}{8d^3} \ll \lambda \quad \rightarrow \quad d \gg \sqrt[3]{\frac{[(x_R - x_H)^2 + (y_R - y_H)^2]^2}{8\lambda}}$$

Therefore, if we use the expression of the development up to the first order for the numerator (most critical factor) and up to the zero order term for the denominator (less critical factor) [21], we obtain, by developing the squares,

$$\mathcal{E}(x_R, y_R) =$$
$$= \frac{e^{i\frac{2\pi}{\lambda}d}}{i\lambda d} e^{\frac{i\pi}{\lambda d}(x_R^2 + y_R^2)} \iint_{-\infty}^{+\infty} \mathcal{R}(x_H, y_H) H(x_H, y_H)\, e^{\frac{i\pi}{\lambda d}(x_H^2 + y_H^2)} e^{\frac{i2\pi}{\lambda d}(-x_H x_R - y_H y_R)} dx_H dy_H$$

This equation is called the Fresnel approximation of the Rayleigh-Sommerfeld integral or *Fresnel transform*. If we now define the variables

$$\mu = \frac{x_R}{\lambda d} \quad , \quad \nu = \frac{y_R}{\lambda d}$$

the previous integral becomes

$$\mathcal{E}(\mu, \nu) = \frac{e^{i\frac{2\pi}{\lambda}d}}{i\lambda d} e^{i\pi\lambda d(\mu^2 + \nu^2)} \iint_{-\infty}^{+\infty} \mathcal{R}(x_H, y_H) H(x_H, y_H)\, e^{\frac{i\pi}{\lambda d}(x_H^2 + y_H^2)} e^{-i2\pi(x_H \mu + y_H \nu)} dx_H dy_H$$

The expression, in this way, has thus assumed, unless the multiplication factor out of the integral not depending on the variables x_H, y_H, the appearance of a two-dimensional Fourier transform and we can therefore write

$$\mathcal{E}(\mu,\nu) = \frac{e^{i\frac{2\pi}{\lambda}d}}{i\lambda d} e^{i\pi\lambda d(\mu^2+\nu^2)} \mathcal{F}\left\{\mathcal{R}(x_H,y_H)H(x_H,y_H)e^{\frac{i\pi}{\lambda d}(x_H^2+y_H^2)}\right\}$$

Where $\mathcal{F}$ denotes the Fourier transform.

It should be recalled, at this point, that, in digital holography, the hologram recording is performed in the digital domain and $H(x_H, y_H)$ is therefore a discretized function; if we assume that the sensor is composed of a rectangular array of M by N pixels with spacing, along the axes $X_H$and Y_H, equal respectively to Δx_H and Δy_H, our hologram appears to be an array of numbers $H(k\Delta \mathrm{x_H}, l\Delta \mathrm{y_H}) = H(k,l)$ and the previous integrals are therefore to be transformed into discrete summations or, equivalently, the continuous Fourier transform has to be replaced by a discrete Fourier transform; the wavefront on the reconstruction plane is then, in turn, a discrete function $\mathcal{E}(m\Delta\mu, n\Delta\nu) = \mathcal{E}(m,n)$ of the discrete variables $m\Delta\mu$, $n\Delta\nu$; taking into account that the maximum spatial frequency is determined by the sampling range in the spatial domain and namely [47]

$$\mathrm{M}\Delta\mu = \frac{1}{\Delta \mathrm{x_H}} \quad , \quad N\Delta\nu = \frac{1}{\Delta \mathrm{y_H}}$$

It is possible to write

$$\mathcal{E}(m,n) = \frac{e^{i\frac{2\pi}{\lambda}d}}{i\lambda d} e^{i\pi\lambda d\left[\frac{m^2}{M^2 \Delta \mathrm{x_H}^2}+\frac{n^2}{N^2 \Delta \mathrm{y_H}^2}\right]} \mathcal{DF}\left\{\mathcal{R}(k,l)H(k,l)e^{\frac{i\pi}{\lambda d}[(\mathrm{k}\Delta \mathrm{x_H})^2+(\mathrm{l}\Delta \mathrm{y_H})^2]}\right\}$$

Where $\mathcal{DF}$ denotes the discrete Fourier transform.

Finally, it can be observed that, according to Fourier transform relationship,

$$\Delta x_R = \frac{\lambda d}{M \Delta x_H} \quad , \quad \Delta y_R = \frac{\lambda d}{\mathrm{N} \Delta y_H}$$

and this means that the reconstructed wavefront in the plane (X_R, Y_R), is represented by a matrix consisting of $M \times N$ elements, each of which is called reconstruction pixel, with dimensions Δx_R, Δy_R. It should be noted that the size of the reconstruction pixels depends on the reconstruction distance because the two expressions correspond to the diffraction limit resolution, for, the optical system as a whole: the hologram constitutes the opening of this optical system and according to the theory of diffraction, the expressions of the values calculated above, Δx_R and Δy_R, correspond to about half the diameter of the Airy disk of the diffraction pattern produced by this opening at a distance d [47].

If we suppose to have a square detector $(M = N)$, with square pixels $\left(\Delta x_H = \Delta y_H = d_p\right)$, we have

$$d_{pr} = \frac{\lambda d}{N d_p}$$

Where $\Delta x_R = \Delta y_R = d_{pr}$

From these expressions it follows that the reconstruction resolution increases when the distance d decreases; unfortunately this distance can't be reduced indefinitely because there will be a minimum value d_{min} for which the maximum angle θ_{max} admitted by the sampling theorem coincides with the minimum value of the angle θ_{min} required to have the diffraction orders separation; in this condition, sketched in figure 1.7, we thus have the maximum resolution for a certain object dimension; working at the minimum distance we thus have

$$\theta = \theta_{max} = \theta_{min} = \varphi = \frac{\psi_{max}}{2}$$

and, consequently

$$\frac{\lambda}{4d_p} = \frac{D+L}{2d_{min}} \quad \rightarrow \quad d_{min} = \frac{2d_p(D+L)}{\lambda} \quad \overset{D \gg L}{\longrightarrow} \quad d_{min} = \frac{2d_p D}{\lambda}$$

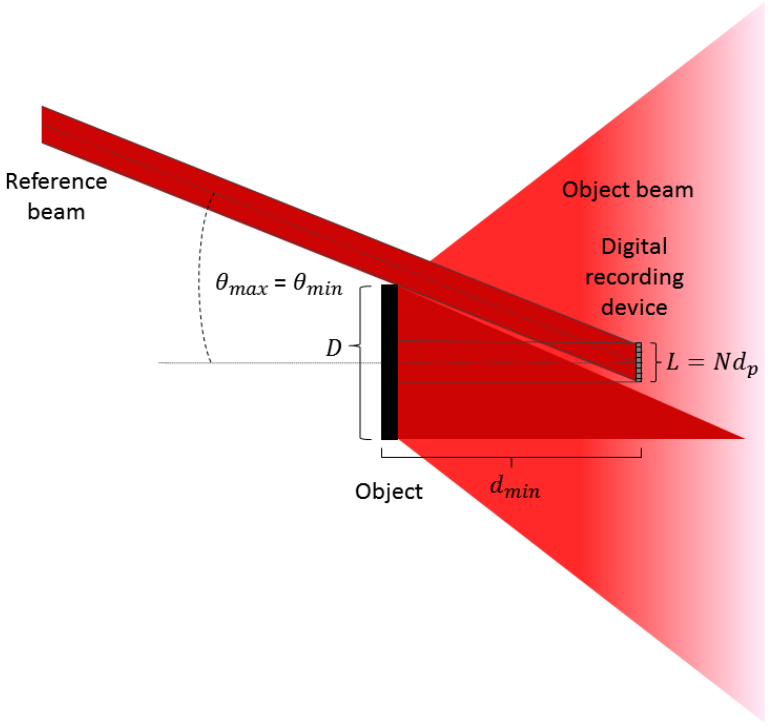

Figure 1.7: Minimum distance configuration.

If we work at the minimum distance the reconstruction pixel pitch becomes

$$d_{pr} = \frac{2(D+L)}{N} = \frac{2D}{N} + 2d_p \quad \overset{D \gg L}{\longrightarrow} \quad d_{pr} = \frac{2D}{N}$$

This means that, at the minimum distance allowed by the sampling theorem, the reconstruction pixel pitch does not depend on the wavelength used to irradiate the object and can't be smaller than the detector pixel pitch. Furthermore, if a large size object, with respect to the detector lateral dimension, is investigated, the reconstruction resolution increases with the number of elements constituting the detector.

Convolution method

The convolution method consists in considering the Rayleigh-Sommerfeld formula for the wavefront reconstruction as a convolution integral, namely

$$\mathcal{E}(x_R, y_R) = \iint_{-\infty}^{+\infty} \mathcal{R}(x_H, y_H) H(x_H, y_H)\, g(x_R - x_H, y_R - y_H)\, dx_H dy_H = [\mathcal{R}\mathcal{H}] * g$$

Where

$$g(x_R - x_H, y_R - y_H) = \frac{1}{i\lambda} \frac{e^{i\frac{2\pi}{\lambda}\sqrt{d^2 + (x_R - x_H)^2 + (y_R - y_H)^2}}}{\sqrt{d^2 + (x_R - x_H)^2 + (y_R - y_H)^2}}$$

Applying the convolution theorem is then possible to write

$$\mathcal{E}(x_R, y_R) = \mathcal{F}^{-1}\{\mathcal{F}\{\mathcal{R}H\}\mathcal{F}\{g\}\}$$

Similarly to the Fresnel method, to make the calculation in DH, we must write the discretized version of this expression and, if the analytical expression of the Fourier transform of the function g is denoted by G, we obtain

$$\mathcal{E}(m, n) = \mathcal{D}\mathcal{F}^{-1}\{\mathcal{D}\mathcal{F}\{\mathcal{R}(k, l)H(k, l)\}G(m, n)\}$$

where [47]

$$G(m,n) = \mathcal{DF}\{g\} = e^{i\frac{2\pi}{\lambda}d\sqrt{1-\frac{\lambda^2\left(m+\frac{M^2{\Delta x_H}^2}{2d\lambda}\right)^2}{M^2{\Delta x_H}^2}-\frac{\lambda^2\left(n+\frac{N^2{\Delta y_H}^2}{2d\lambda}\right)^2}{N^2{\Delta y_H}^2}}}$$

This method does not impose a limit to the distance between the object and the sensor during the hologram recording process but requires the calculation of a Fourier transform and of an inverse Fourier transform.

In this case the reconstruction pixels pitches, because of the double Fourier transform, are

$$\Delta x_R = \Delta x_H \quad , \quad \Delta y_R = \Delta y_H$$

These expressions could suggest that, by this method, the reconstruction pixels pitches have the same dimensions as the camera pixels, that is, for $d > M\Delta x_H^2/\lambda$, $N\Delta y_H^2/\lambda$, smaller than the values obtained by the Fresnel method; actually the reconstructed image resolution is still, at most, the resolution given in the formula of Fresnel method, as imposed by the diffraction limit, but, in this case, only a small portion of the object, equal to the size of the sensor, is played back; to obtain a complete reproduction of the object it is possible to use various techniques: it is possible to exploit the so-called *zero padding* technique, which substantially consists in adding a frame of zeros around the hologram matrix in order to perform the reconstruction of a greater size matrix (the greater the synthetic matrix the greater the reconstructed portion of the object) [27;28]; alternatively it is possible to use a so-called *numerical lens*, i.e. to multiply the matrix of the hologram by an appropriate mathematical factor that reproduces the effect of demagnification of the field of view that would be achieved by the introduction of a lens in the real system [47;52];

another possibility is to reconstruct different portions of the object wavefront introducing a shift in the function $G(m,n)$ and then stitching them together [47].

Lensless Fourier Holography

When a lensless Fourier holography configuration is employed the Fresnel transform simplifies significantly; the reconstructed wavefront in the sensor plane in this case is describe by

$$\mathcal{R}(x_H, y_H) = \frac{e^{-i\frac{2\pi}{\lambda}\sqrt{d^2+{x_H}^2+{y_H}^2}}}{\sqrt{d^2+{x_H}^2+{y_H}^2}} \cong \frac{e^{-i\frac{2\pi}{\lambda}d}e^{-i\frac{\pi}{\lambda d}({x_H}^2+{y_H}^2)}}{d}$$

When this expression is inserted in the reconstruction formula the Fresnel transform reduces to

$$\mathcal{E}(\mu,\nu) = Ce^{i\pi\lambda d(\mu^2+\nu^2)} \iint_{-\infty}^{+\infty} H(x_H, y_H)\, e^{-i2\pi(x_H\mu+y_H\nu)} dx_H dy_H =$$
$$= Ce^{i\pi\lambda d(\mu^2+\nu^2)} \mathcal{F}\{H(x_H, y_H)\}$$

Where C is a complex constant.

A lensless Fourier hologram is therefore reconstructed by a simple Fourier transform of the hologram function. Furthermore, when a lensless Fourier holography configuration is employed, it is no longer possible to focus on different areas within the object volume since the distance d does not enter any more the Fourier integral; this means that in the reconstruction algorithm the distance d do not appear anymore and, consequently, in a lensless Fourier hologram reconstruction both diffracted orders appear in focus.

Undiffracted term suppression

There exist different methods to remove the undiffracted term in DH [47]. As we have seen, the expression of the intensity recorded on the hologram is

$$I(x,y) \propto E_o^2(x,y) + E_r^2 + 2E_o(x,y)E_r \cos\left[\phi_r(x,y) - \phi_o(x,y)\right]$$

The first two terms of this expression give rise to the undiffracted disturbance term while the third term contains the information we are interested in.

The most direct, but more laborious, technique to eliminate the effects of the first two terms of this expression from the reconstructed one, consists in acquiring three different images: the interferogram, the reference beam only and the object beam only; these images can be acquired from time to time by blocking the beam we are not interested in; subtracting from the image of the hologram the other two images an undiffracted term free image is obtained.

If we are not willing to acquire more than one image, we can use the *subtraction of the mean value* method: the third term of the reconstructed wavefront is statistically varying between $\pm 2E_o(x,y)E_r$ from pixel to pixel at the recording device; the first two terms can then be suppressed by subtracting the average intensity of the hologram matrix from all the elements of the hologram matrix itself.

A similar effect can be achieved if two holograms with stochastically changed speckle structures are subtracted from each other and the reconstruction of this difference is performed.

Alternatively, similarly to the case of analog holography, the elimination of the undiffracted terms can be obtained by cutting the undesired components from the spectrum of the signal; this result can be obtained in DH, numerically, in two ways: a first method consists in performing the Fourier transform of the signal, detect the noise components, remove them with appropriate filters and finally antitransform to obtain the hologram relative to the signal of interest. A second method consists in applying a high pass frequency filter or, preferably, a band-pass filter to the hologram

itself, possibly after adjusting the parameters according to the information provided by the Fourier transform of the signal. The last method, based on more sophisticated filters, has been applied in all the hologram reconstructions performed in our experiments.

1.2.3 Advantages of digital holography

DH is characterized by a series of interesting characteristics that make it more appealing with respect to its classical counterpart and with respect to most standard imaging techniques; thanks to these characteristics it can be of interest in many different applications and it is therefore meeting growing interest.

The fundamental aspect that differentiates DH with respect to standard imaging techniques is the possibility to reconstruct both the amplitude and the phase images of the sample under examination; this information, of great interest in a wide variety of applications, is obtained with a minimally invasive technique since the remarkable sensitivity which characterizes modern recording digital devices allows, if necessary, to use very low power laser radiation during the hologram recording process. Another interesting characteristic of DH is the possibility to perform, with a single acquisition, the reconstruction of the object image at different distances; this means that focusing on particulars belonging to different planes that make up the scene, can be obtained numerically during the reconstruction process starting from a single recorded hologram. Furthermore, as in classical holography, each portion of an hologram carries the information of the entire sample and can be used to retrieve it; this means that even if part of the sensor is covered during the recording process it is still possible to recover the information about the entire scene under investigation.

Many advantages characterize DH with respect to analog holography. First of all the digital hologram recording process is by far faster and easier than its analog counterpart: no delicate and time consuming photographic recording and development processes are required. Moreover, the times required for numerical

reconstruction are today, with a modern computer, in the order of a second and do are not a limitation in most applications.

In addition to these important basic features of DH there is the possibility, through various techniques, instrumental or strictly numeric, to improve the quality of the final reconstructed image. It is possible, among other things, to improve the image resolution through the use of numerical zero padding technique [16] or through various different recording techniques [45], to enlarge portions of the image with the use of numerical lenses [52], to correct numerically aberrations of any lens used [49], to obtain an extended focus image of the sample [17], to correct the noise introduced by dust and inaccuracies in the alignment of the optics, by means of average procedures over a large number of acquisitions.

2 Infrared digital holography

The idea behind holography (both in its analog and digital version), that is to record and subsequently reconstruct the amplitude and phase information of the wavefront under investigation, is so general and rich in applications to be of interest in all regions of the electromagnetic spectrum. Obviously, the different wavelengths require different recording devices and the inhomogeneous technological development of the various acquisition devices has inevitably benefited certain regions of the spectrum with respect to others. In DH, for example, infrared (IR) sources were penalized, compared to visible sources, due to the critical issues related to the detection of this kind of radiation. However, increasing interest toward standard IR imaging techniques, firstly related to their military, industrial and thermal efficiency applications, has boosted the production of thermographic cameras and the availability of such IR cameras, based on the latest sensors generation, represents a significant stimulus to the development of DH techniques also in this region of the electromagnetic spectrum. This renewed interest could lead to innovative applications in security screening, night vision, and biological science, as it can extend holographic 3D imaging capabilities from visible to IR spectrum, up to the terahertz frequencies.

2.1 Infrared radiation, sources and detectors

Infrared radiation

The IR range extends from about $0.750\mu m$ up to about $1000\mu m$. The IR window is usually conventionally divided into three different regions: ***Near IR*** $(0.750\mu m - 3\mu m)$, ***Mid IR*** $(3\mu m - 30\mu m)$, ***Far IR*** $(30\mu m - 1000\mu m)$. These boundaries are indeed not so firmly fixed and many other classifications do exist. The Mid IR region is sometimes called *thermal infrared* (and also *long-wavelength infrared*) while the Far IR region is nowadays commonly called *Terahertz* region (or *T-ray* region). Infrared

radiation is used extensively in industrial and scientific applications such as environmental monitoring, industrial facility inspections, surgery, temperature sensing and spectroscopy. In most cases the above applications are based rather on Near and Mid IR radiation, due to the availability of efficient sources and detectors in these frequency ranges. On the contrary, the terahertz band, which lies between the optical and the microwave spectrum, is still almost unexploited and is currently one of main research topics in optics because of its numerous and promising possible applications. In this work we restricted the research field just to the longer wavelength of the Mid IR and Far IR radiation because of their attractive features with respect to DH employment.

Sources

The Mid IR experiments developed in this thesis were based on a well assessed ***Carbon Dioxide (CO_2) Laser*** [40] because of the high versatility of this kind of coherent source: CO_2 lasers, in fact, are able to operate either pulsed or continuously with very high overall efficiency (up to 20%) and can produce continuous wave radiation ranging from few milliwatts up to more than $10kW$ power (nowadays the highest power achievable with a commercial laser). They are based on a set of $C0_2$ vibrational rotational transitions enabling them to emit from $9\mu m$ to $11\mu m$; they can operate simultaneously on many lines or be tuned to a single wavelenght with very long coherence lengths (up to several meters). The laser active medium is excited by an electric discharge passing through the laser gas, which contains, besides carbon dioxide, also nitrogen (N_2) and (usually) helium (He). Both N_2 and $C0_2$ molecules absorb energy from electrons in the discharge but the lowest vibrational level of N_2 easily transfers energy to $C0_2$. Helium helps to maintain the population inversion by facilitating $C0_2$ molecules to drop from the lower laser levels to a lower level or to the ground state. Due to the high output powers that $C0_2$ lasers can reach, they are commonly used in cutting and welding industrial metal profiles and, due to the strong absorbance of water inside tissues at these wavelenghts, they are frequently

employed in surgery and dermatology. A major drawback of this kind of lasers lies in their considerable size which, obviously, limits significantly the possibility to move out of the laboratory the techniques developed in this thesis using these sources. In this respect a promising alternative to CO_2 lasers is offered by a much more recent and extremely compact kind of lasers, operating both in the Mid IR and in the Far IR range, *Quantum Cascade Lasers*.

The idea at the basis of ***Quantum Cascade Laser (QCL)*** working principle was firstly proposed in 1971 [25] but it was only in 1994, thanks also to the development of innovative atomic layer growing techniques, like molecular beam epitaxy (MBE) [9], that such a novel kind of semiconductor laser saw its first realization at Bell Labs [15]. Unlike typical interband semiconductor lasers which emit electromagnetic radiation through the recombination of electron-hole pairs across the material band gap, in QCLs the laser transition occurs between quantized electronic energy levels (subbands) within the conduction band of a repeated stack of multiple semiconductor quantum wells; as a consequence, the emission wavelength is not determined by a particular transition intrinsic to the material which constitutes the active medium, but can be tailored by acting on the quantum confinement characteristics; a broad wavelength range can therefore be covered, e.g., by tuning the thickness of the individual layers comprising the structure, without changing the materials composition. QCLs are called *unipolar* devices in that only the electrons are involved in the radiating process: every time an electron traverses the lasing medium it moves from one quantum well to the next, driven by the voltage applied across the device and, at precisely engineered locations, called *active regions*, it passes from one conduction band energy state to a lower one thus emitting a photon. Additionally, while in semiconductor laser diodes, electrons and holes are annihilated after recombining across the band gap and can play no further part in photon generation, in a QCL, once an electron has undergone an intersubband transition and emitted a photon in one period of the structure, it can tunnel to the upper laser state of the following period where another photon can be emitted. This process of a single

electron causing the emission of multiple photons as it traverses through the QCL structure gives rise to the term *cascade*. In this multistage cascade scheme (figure 2.1), electrons are recycled from period to period, contributing each time to the gain and to the photon emission. Each stage belonging to the cascaded repetition consists of an *active region* followed by a *relaxation-injection region*. The electrons in the injection region are transferred by quantum mechanical tunneling to the excited state of an adjacent quantum well. Emission of radiation is a consequence of the electron relaxation to the ground state of the same quantum well (vertical transitions) or to that of the next one (diagonal transitions). To sustain population inversion, the ground level of the radiative transition must be depleted by fast carrier transfer to the following electronic injector stage (i.e., via resonant optical phonon emission). Sequential repetition of these two regions allows electrons to be recycled from one stage to another, taking to the emission, in principle, of as many photons per electron as the number of stages in the laser structure leading to a quantum efficiency much larger than one.

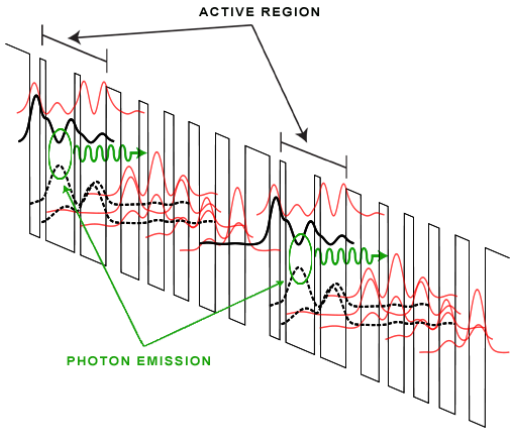

Figure 2.1: Typical scheme of quantum cascade laser structure.

Since the first realization in 1994, QCLs have experienced a remarkable development and, today, as previously stated, QCLs are fruitfully employed both in the Mid IR and

in the Far IR, from 2.6μm [6] up to 250μm (1.2THz) [56], with lasing demonstrated in both InGaAs/AlInAs and GaAs/AlGaAs material systems; an emission wavelenght encompassing a two orders range represents a really remarkable result, especially if it is considered that this broad operating range is obtained with the same lasing principle. It exists, however, a significant gap between Mid IR and Far IR QCLs performances. In particular, QCLs now represent the highest performing lasers available in the MIR frequency: they can operate almost continuously from 2.6 μm to 24 μm [10] delivering several watts of optical power in pulsed mode and several hundred milliwatts in continuous mode [2]; Mid IR QCLs can operate above room temperature in pulsed mode in a wide range of wavelenght (5$\mu m - 12\mu m$) [14] and at room temperature in continuous wave for specific wavelenghts [3].
In the THz spectrum, QCL operation was firstly demonstrated in 2002 [26], and, at present, THz QCLs continuously cover the $1.2 - 4.5THz$ range. Since their first experimental demonstration, THz QCLs have undergone significant progress with the development of specific active region designs (*chirped superlattice*, *bound to continuum* and *resonant phonon*) but can still operate only at cryogenic temperature with a maximum output power of 250mW, in pulsed mode, and 130mW in continuous wave mode [58].

Detectors

As we have seen in the first chapter, array sensors are needed to perform DH and, among the most common IR sensors, we opted for pyroelectric and microbolometric sensors (most of which were already available in our laboratory).
Pyroelectric sensors [29] are based on the ability of some materials (such as LiTaO3) to generate an electric potential when they are momentarily cooled or heated; the temperature change induced in these crystals, slightly modifies the orientation of the molecular electric dipole moments within the crystal structure, producing a variation of the polarization of the material; this variation, in turn, gives rise to a local electric potential that is possible to reveal and that disappears after a short relaxation time;

these sensors do not require cooling systems and are usable throughout the infrared region. ***Microbolometric*** sensors [46] are based on the properties of some materials (such as amorphous silicon, aSi, and vanadium oxide, VaO) to change the value of its electrical resistivity by virtue of a rise in temperature; these sensors do not require cooling system and are able to work in a rather high range of wavelengths typically going from $8\mu m$ up to the Far IR with appropriate processing; thanks to their reduced dimensions, microbolometric sensors allow to obtain very high resolution images, not achievable with other types of sensors and are therefore optimal devices for DH applications.

2.2 Advantages and disadvantages of IR DH

Our decision to use long wavelenght radiation to perform DH is related to some intrinsic characteristics of this technique. First of all, as we have already mentioned, the radiation wavelenght does not enter into the expression for the reconstruction pixel pitch when operating at the minimum distance admitted by the sampling theorem; the reason for this unexpected property resides in the fact that, according to the general expression of the reconstruction resolution, the longer the wavelength in use the larger should be the reconstruction pixel size (the worse the resolution) but, if we look at the expression of the maximum angle between object beam and reference beam, we see that a longer wavelength allows to work at lower object-camera distances thus compensating what was lost in terms of resolution. Reconstruction pixels pitch is indeed rather heavily dependent on the number and size of the elements constituting the recording device. In the past, infrared detectors were characterized by a number of sensitive elements much lower than the detectors in the visible range and, at the same time, the size of the sensing elements was much larger than those of typical CCDs; probably this deficiency in IR detection devices, combined with the ease of use of visible radiation, prevented, in the past, a significant development of DH techniques at these wavelengths. Today the situation is greatly

improved even if the gap between the performances of infrared sensors and visible ones is not yet completely filled: ***Thermoteknix MicroCAM 1024HD***, a high-level commercial uncooled long wavelenght detector, has a 1024×768 elements with $17\mu m$ of lateral dimension, ***NEC IRV-T0831***, a high level commercial uncooled Terahertz detector has 320×240 elements with $23.5\mu m$ of lateral dimension, ***Hamamatsu ORCA-Flash4.0***, a high-level commercial visible camera, has 2048×2048 elements with $6.5\mu m$ of lateral dimension. With the expected progress of IR detection technologies, especially if we consider the significant current interest in the IR region, it is reasonable to assume that these values are going to be soon overcome so that the resolution gap between visible detectors and IR detectors are intended to get thinner and thinner. With these typical sensors technical values in mind it is simple to evaluate advantages and disadvantages of Infrared DH (IRDH) with respect to visible DH: with reference to table 2.1 it is evident that, for a fixed object dimension D, IR radiation is the best choice if large size objects are of interest, even if a slightly lower resolution is obtained.

Source	CO_2 laser	Quantum Cascade Laser	Solid State Laser
Wavelenght	$10.6\mu m$	$111\mu m$	$0.532\mu m$
Detector active pixels	1024×768	320×240	2048×2048
Detector pixels size	$17\mu m$	$23.5\mu m$	$6.5\mu m$
$\boldsymbol{d_{min} = \frac{2d_pD}{\lambda}}$	$3.2D$	$0.42D$	$24.4D$
$\boldsymbol{d_{pr} = \frac{2D}{N}}$	$0.002D \times 0.003D$	$0.006D \times 0.008D$	$0.001D \times 0.001D$

Table 2.1: Typical hologram recording and reconstruction parameters in the Mid IR, in the Far IR and in the Visible region for a large size object of lateral dimension D.

As shown in the table, in fact, an object with $1m$ lateral dimension, for example, must be at least $24m$ away from a visible detector while it could stay at about $3m$ if CO_2

radiation is used and even less than $0.5m$ if we are working in the Terahertz region. The reconstruction resolution, instead, remains of the same order in all cases.

There is, however, also an intrinsic advantage in using long IR radiation in DH, and, more generally, in every interferometric experiment, that is the inherent lower sensitivity to vibrations of long wavelenght radiation. Optical path variations due to seismic noise or to any other vibration source, in fact, determine a lower phase variation between the reference beam and the object beam, the longer is the wavelenght used to create the interference pattern. This benefit makes less critical the stability of the object and of the measuring apparatus in general, during the holograms acquisition and is thus strongly indicated for DH, particularly in the investigation of large size objects. IR radiation makes it possible to work thus in less restrictive conditions allowing to operate even out of the laboratory, giving much more versatility to the technique and opening the way to many possible applications out of the laboratory. By means of long wavelenght radiation it is also possible to create video holograms (meaning holographic video of slowly changing dynamical scenes) without using a pulsed laser and short acquisition times necessary if working with visible radiation. When very large size samples analysis is needed, CO_2 laser radiation is strongly recommended since the high output power that CO_2 lasers can reach, is needed to irradiate efficiently large object surfaces (such high power beams can in fact be expanded, through suitable optical systems, up to cover the entire surface of the object under study and ensure a sufficient power value all over the sample). Furthermore the very high coherence length typical of CO_2 lasers represents certainly an important advantage in every interferometric applications. All these features make CO_2 lasers highly recommended if you need to use DH to investigate large size objects in out of laboratory applications.

Among the reasons that may encourage the use of IR in DH there is also the transparency of various materials at certain wavelengths in the IR spectrum; this property can be exploited to study internal structures of such materials at different depths, to investigate heterogeneous materials or in security and safety applications.

As we will see Mid IR radiation is highly transmitted through smoke while Far IR is well known for its capability of passing through plastic materials, clothes, paper, wood and many other materials. Unfortunately water is strongly absorbed both at $10.6\mu m$ and in the Terahertz region and, consequently, exploitation of these wavelenghts for biological purposes is restricted to thin samples investigation.

3 Experiments with Mid IR digital holography

As anticipated, the first experimental part of this work was devoted to DH in the Mid IR and, more precisely, using the 10.6μm radiation produced by a CO_2 laser. Mid IR DH is gaining momentum thanks to its applications in the field of non-destructive testing analysis of large samples and in the field of real 3d imaging, and, as we will see, future applications could originate on the basis of some of the results obtained during this PhD project.

3.1 Experimental apparatus

As we are going to see in detail, the experimental apparatus needed to perform Mid IR DH is quite simple: all it is needed is a Mid IR coherent source, an appropriate array detector and few specific optics elements (beam splitters, lenses and mirrors). Further instruments, like Spatial Light Modulators, motorized stages and special optics were employed for other applications and are described when needed.

The laser used throughout our experiments was a CO_2 laser, Blade 100 by EL.EN Spa, emitting linearly polarized radiation at 10.59μm, relative to the line P(20), in continuous mode, on the Gaussian fundamental TEM00 mode, up to a maximum power of 130W; the laser beam was characterized by a minimum diameter, beam waist, at the output of the resonant cavity, of about 10mm and a divergence of about 2.2$mrad$. Using this kind of laser (belonging to the class IV) requires maximum attention both for the presence of a high power supply voltage (about 11kV) and for the risk of eyes or skin exposure to direct beam or to diffused radiation by obstructions on the path of the laser. To safely perform the alignment of the optical system we used a pointing source (laser diode at 670nm wavelength) previously calibrated so as to follow the same path of the main laser beam.

The detector used throughout our experiments was a microbolometric camera, by Thermoteknix, with the characteristics shown in table 3.1.

	Thermocamera Thermoteknix
Model	$Miricle\ 307K-25$
Detector material	$Amorphous\ Silicon$
Array size	640×480
Pixel pitch	$25\mu m \times 25\mu m$
Spectral response	$8\mu m - 12\mu m$
Sensitivity	$\leq 70mK$
Frame rate	$50\ frame/s$

Table 3.1: Thermocamera specifications.

The thermocamera, as in every holographic setup, was used in its lensless configuration. The software accompanying this camera allows to acquire single images in different formats but also live video in the format *.avi. The acquired holograms, or video hologram, were numerically processed by means of 'home made' algorithms working in Matlab environment. All tested configurations were arranged on a vibration isolated table by Melles Griot (used, for our purpose, not in vibration isolated condition). Since standard glass is not transparent at this wavelenght special Zinc Selenide (ZnSe) optics and gold coated plane mirrors were used.

3.2 Experimental setups and results

The very first results in IRDH at $10.6\mu m$ were obtained in 2003 by a INO group [1] using a CO_2 laser with $190mW$ power and a pyroelectric camera, Pyrocam III by Spiricon, with 124×124 $LiTaO_3$ elements with pixel size $85\mu m \times 85\mu m$ and centre to centre spacing of $100\mu m \times 100\mu m$. In this first experiment a transmission holographic configuration was realized; with the setup illustrated in figure 3.1 the

wavefront transmitted through a drilled metallic plate was recorded and numerically reconstructed both in amplitude and phase (see figure 3.2).

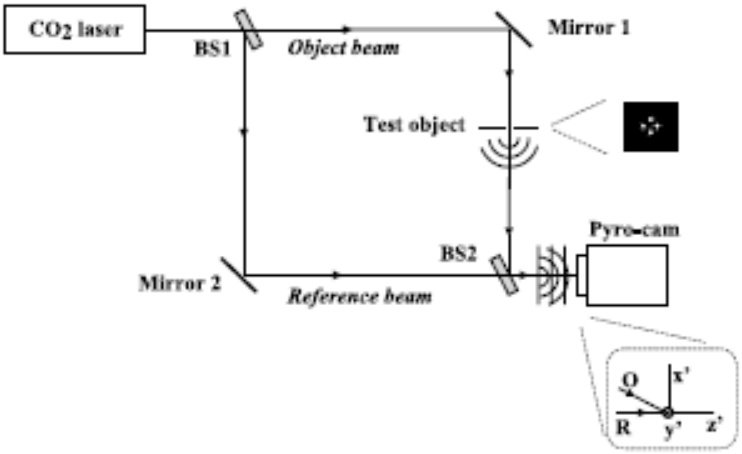

Figure 3.1: Transmission holography setup. BS1 and BS2 are 50/50 ZnSe beam splitters.

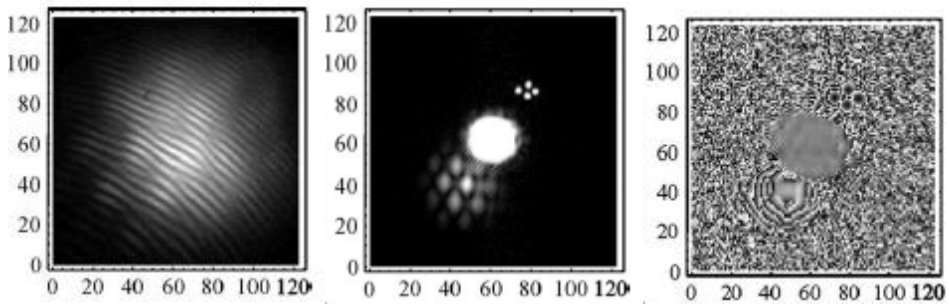

Figure 3.2: (From left to right) Hologram; amplitude reconstruction; phase reconstruction.

In 2008 the same INO group, with a slightly more powerful CO2 laser ($800mW$) and the same Pyroelectric camera, by means of a reflection holographic setup (figure 3.3), managed to record and numerically reconstruct both the amplitude and phase of the wavefront reflected by small (1inch diameter) metallic objects [11] (figure 3.4).

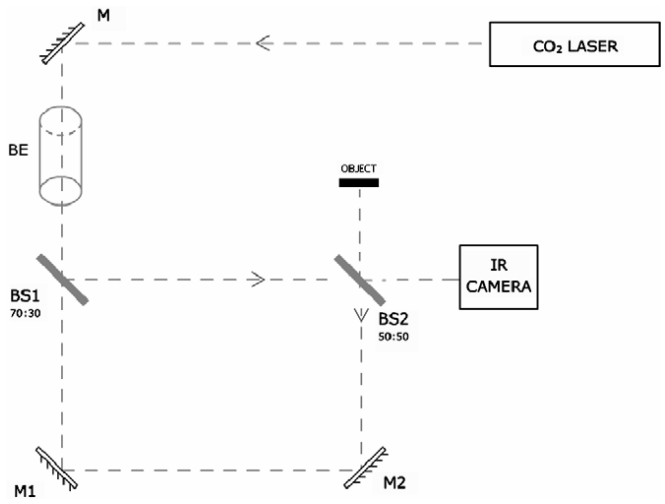

Figure 3.3: Reflection holography setup. BS1 and BS2 are ZnSe beam splitters; M, M1 and M2 are plane mirrors, BE is a ZnSe beam expander.

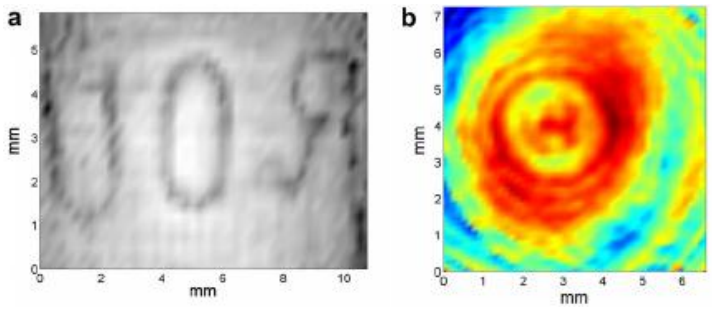

Figure 3.4:.(From left to right) Amplitude reconstruction of an inscription on a metallic plate; phase reconstruction of a circular metallic disc with circular patterns inscribed.

3.2.1 First results

When I started to work in this field, in collaboration with the same INO group which had realized the above experiments, our first efforts were dedicated to the improvement of previously obtained results [44;43]; we thus decided to move to speckle IRDH in order to investigate higher dimension scattering objects. As we have already said, larger samples means longer object–detector distances and, consequently, lower reconstruction resolutions; in order to reduce this resolution loss we bought a higher resolution, larger size and more sensitive detector, the microbolometer detector Miricle 307K described in the previous paragraph; in order

to guarantee a more efficient object irradiation we opted for the $100W$ CO_2 laser available in our laboratory. The optical configuration used in these first experiments (figure 3.5) is a typical DH setup and was used as starting point for all the other configurations employed throughout our experiments; in what follows we will refer to this arrangement as to the *basic configuration*.

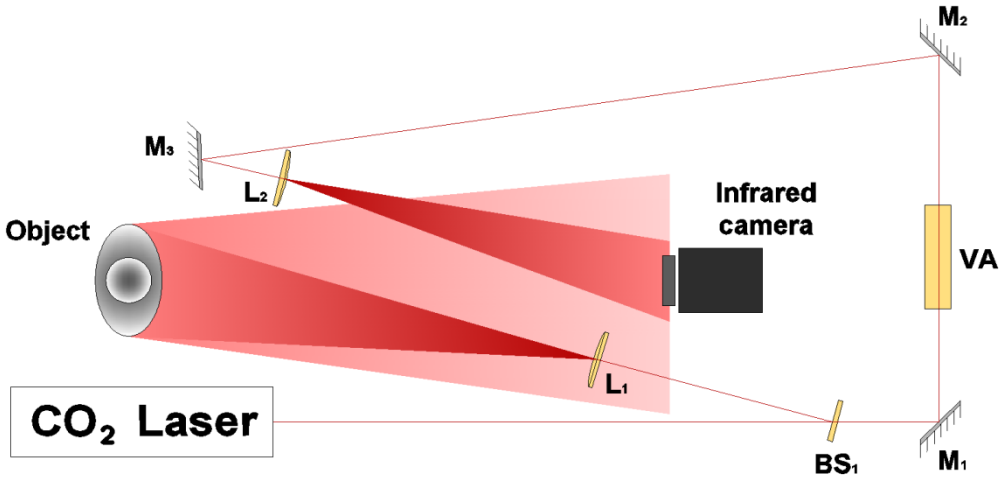

Figure 3.5: Basic digital holography configuration. M1, M2 and M3 are plane mirrors; BS1 is a ZnSe 80/20 beam splitter; L1 and L2 are ZnSe 1.5 inch focal length spherical lenses.

In this setup the CO_2 laser beam is first divided by a ZnSe beam splitter (BS1) which reflects 80% of the impinging radiation and transmits the remaining 20%. The transmitted part, which constitutes the reference beam, is reflected by means of a plane mirror (M1) towards a ZnSe variable attenuator (VA); the reference beam is then redirected by means of other two plane mirrors (M2, M3) toward the thermocamera but, before impinging on the detector, it encounters a ZnSe converging lens of 1.5 inch focal length (L2), which focus and then enlarges it in order to reach the thermocamera with enough low intensity and an almost planar wavefront. The reflected part of the fundamental beam constitutes indeed the object beam; before impinging on the sample it passes through a ZnSe converging lens of 1.5 inch focal length (L1), which focus and then enlarges the beam so as to irradiate a more or less

large surface of the object depending on its distance from the sample. The interference pattern created by the object beam and the reference beam across the sensor is optimized, in order to increase the fringes visibility, acting on the reference beam intensity by means of the variable attenuator. The hologram can be collected and digitally stored in a computer both in the form of a single image and in the form of a video if a dynamical scene is of interest. Thanks to the low sensitivity to vibration of the whole system the antivibration modality of the table is not activated during the experiments. Since the detector is only sensitive to IR radiation artificial lights or sunlight is not disruptive. Usually the sample is positioned just in front of the detector and so great attention has to be done in the positioning of the mirror M3 because its position determines the angle between the reference beam and the object beam and, ultimately, the fringe spacing; as we have seen in chapter 1, it is necessary to vary the inclination between the two beams so as to obtain a sufficiently high fringes spatial frequency to separate the real image from the virtual one, without, however, breaking the limits imposed by the sampling theorem. When working with such high-power laser, special attention must be paid not to inadvertently send toward the sensor a too high reference beam which, considering the high sensitivity of this kind of detector, and its low damage threshold, would permanently injury it.

In the first holograms recorded with this configuration we used, as object, a small bronze statue reproducing emperor Augustus (figure 3.6), about $10cm$ high. In figure 3.6 the acquired hologram and its amplitude reconstruction are shown too. For completeness, the real reconstructed image, comprehensive of both diffraction orders, is shown in figure 3.7 (from now on we will omit to show both orders in next reconstructions). Both orders are in focus because, in this case, a lensless Fourier holography configuration was used.

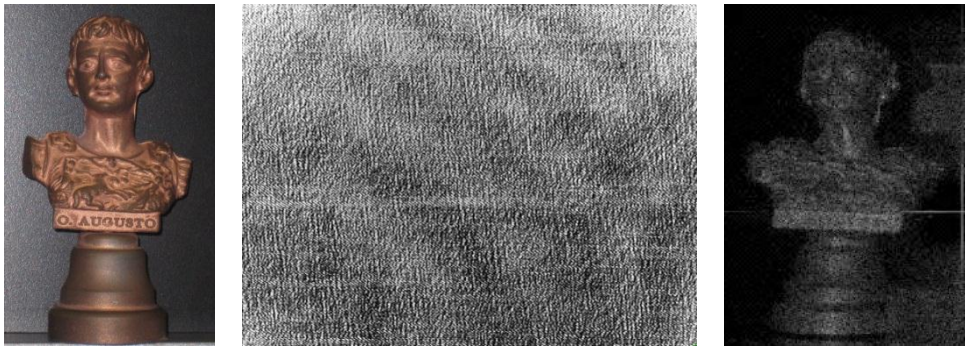

Figure 3.6: (From left to right) Augustus small statue; Augustus IR hologram; Augustus numerically reconstructed hologram

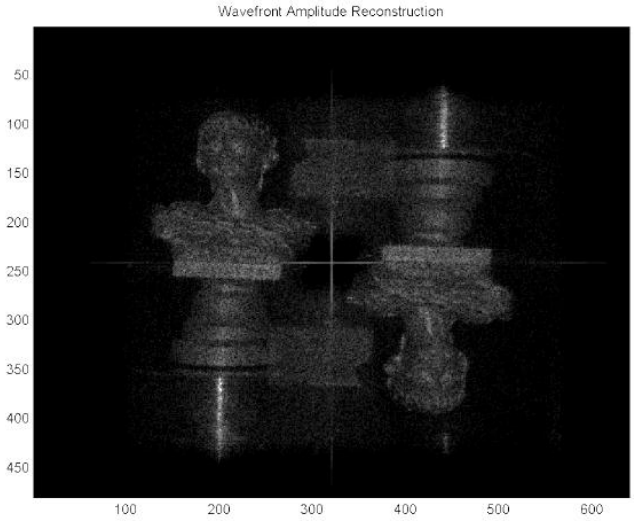

Figure 3.7:.Augustus numerically reconstructed hologram (both diffraction orders visible)

A second and larger size statuette (34cm high) reproducing Benvenuto Cellini's Perseus sculpture has been successfully investigated with the same configuration; in figure 3.8 a photo of the statue, the relative hologram and the reconstructed amplitude wavefront are shown.

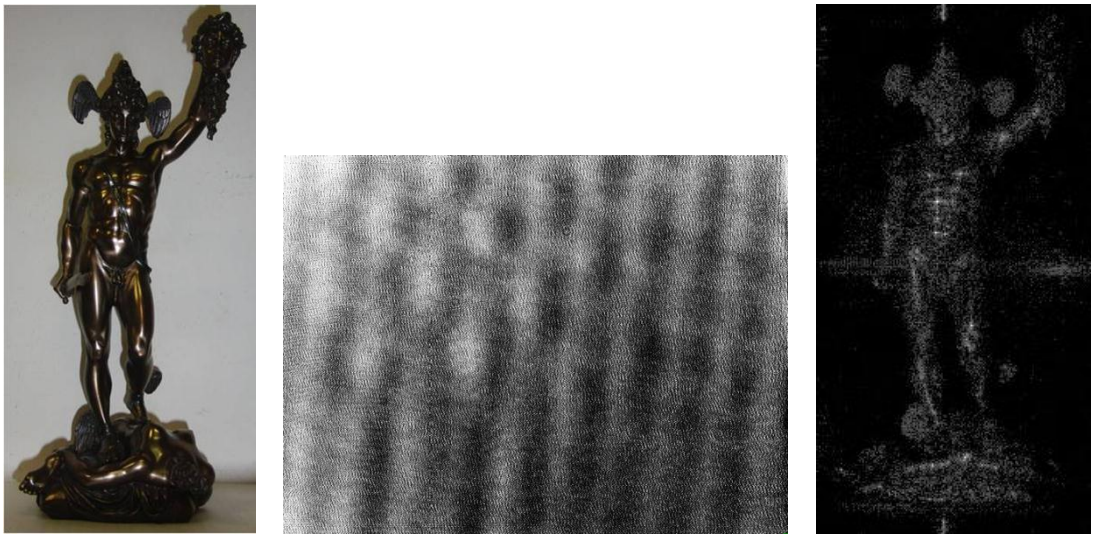

Figure 3.8: (From left to right) Perseus statue; Perseus IR hologram; Perseus numerically reconstructed hologram.

As we have anticipated, thanks to the lower vibration sensitivity of $10.6\mu m$ DH we were able to acquire, and successfully reconstruct, video holograms of dynamical scenes in CW laser condition. To test this possibility we positioned the sample on a motorized stage so that it could rotate on itself at low angular velocity (around 360°/minute) and obtained a high quality video reconstruction (video 1). When higher angular velocities are employed the fringe visibility decreases progressively and the reconstruction resolution gradually reduces; a higher frame rate and a shorter exposure time would be necessary to sample effectively the interference pattern and freeze the fringes in good visibility conditions. Our thermocamera could not acquire more than $50 frame/s$ but higher frame rate thermocameras (up to $240 frame/s$) are already commercially available.

3.2.2 Super resolution by means of synthetic aperture

Since our detector elements were larger and less numerous than typical visible detector elements our first results lacked of resolution with respect to typical visible holograms. One of the first improvements we decided to pursue consisted thus in increasing our holograms resolution [45]. Since hologram dimension (that is the

detector surface) enters at the denominator in the reconstruction pixel pitch expression and since the detector surface is significantly smaller than the interferometric pattern surface created in air by the object beam and the reference beam interference, we decided to increase synthetically the numerical aperture of the system by means of an automatic technique capable of recording several shifted but partially superimposable holograms and stitching them together. To achieve this result we exploited the basic DH configuration but fixed the thermocamera at two motorized translational stages, LTS300 by Thorlabs (figure 3.9).

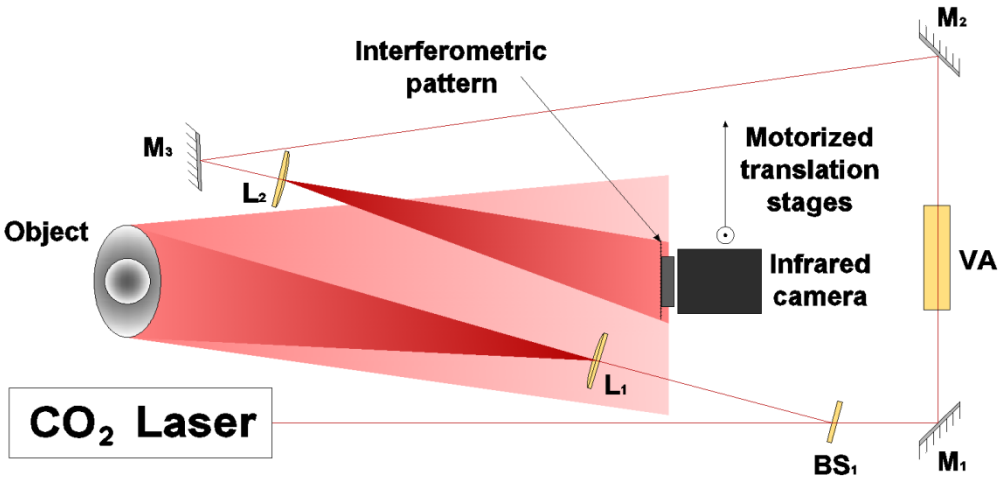

Figure 3.9:.Holographic setup for shifted holograms acquisition.

By means of a remotely controlled routine it was thus possible to move the sensor horizontally and vertically along a serpentine path on the hologram plane and acquire various equally spaced, minimally overlapping, portions of the large interferometric pattern. The recording session had to be completed in a relatively short time so as to minimize changes in the interferential pattern even if the task was facilitated by the low vibration sensitivity of long wavelenght radiation. The numerous holograms thus recorded were then stitched together by means of an automated algorithm developed by our group, obtaining a digital hologram with a synthetic but larger numerical aperture. The stitching procedure, called *registration*, is a standard image processing

technique to determine the geometrical transformation that aligns points in one picture with corresponding points in another picture. Often, the registration is performed manually or in a semi-automatic way by a user iteratively setting the parameters of the geometrical transformation. However, this approach is time consuming and can give subjective results. On the other sides most of totally automated algorithms are not always applicable to align and stitch speckle holograms, which, due to their apparently random and very fine pattern and due to the inevitable inherently differences of the images structures and tone dynamics, are hard to match and experimentally result in noisy images. We thus decided for a specific automated method based on the maximization of the mutual information (MMI) [33], which was capable of taking into account any possible shift, rotation and scaling among the different holograms and that has shown excellent results compared to the other methods.

We decided to test this procedure to improve the reconstruction resolution of the previously investigated samples, Augustus and Perseus. In particular, a synthetic hologram composed of 7×3 standard holograms was employed to obtain the synthetic hologram and its relative amplitude reconstruction of Augustus image while a 4×3 synthetic hologram was employed for Perseus image. The quite encouraging results are shown in figure 3.10 and 3.12.

Again the high power of our CO_2 laser revealed as an advantageous parameter helping to obtain a larger interferential pattern with respect to standard visible pattern, and therefore allowing acquiring a larger number of single holograms to be stitched together. The reconstructed image resolution however cannot increase indefinitely because when the synthetic aperture hologram reaches a certain dimension the reconstructed wavefront curvature, corresponding to different perspectives, cannot be properly represented with a 2D numerical reconstruction. The different perspective views written in the synthetic aperture hologram become evident if two

different portions of the hologram (the left half and the right half part for example) are reconstructed and shown alternatively (video2).

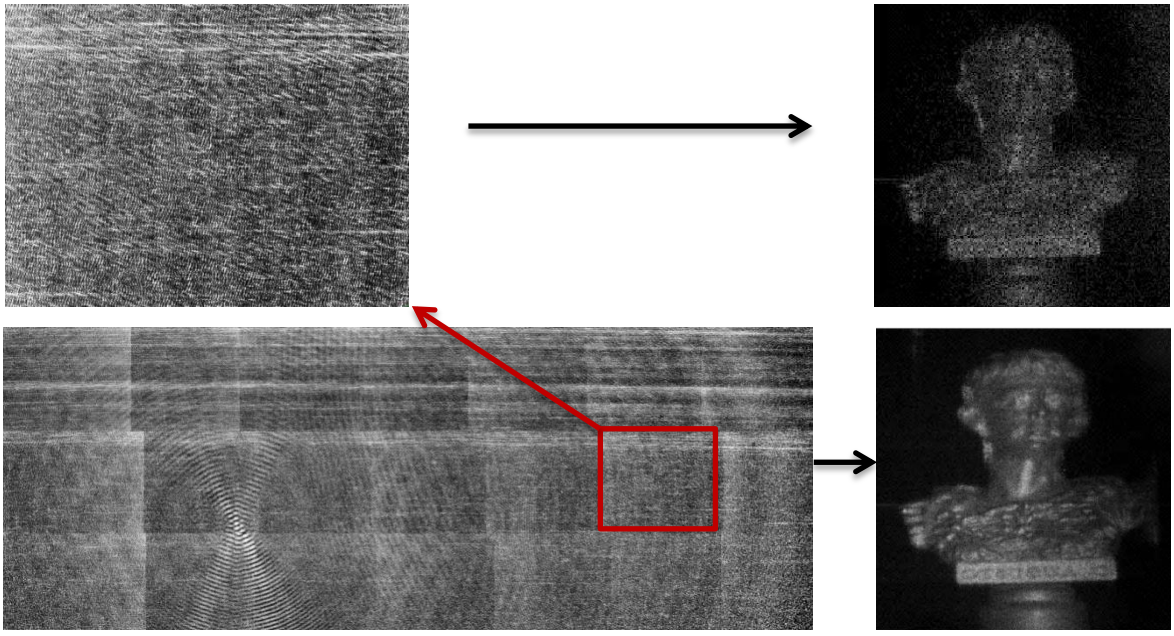

Figure 3.10:.Augustus hologram stitching. (From left to right) Single hologram and single hologram amplitude reconstruction; 7 × 3 stitched holograms and stitched holograms amplitude reconstruction.

Noteworthy, the enhanced resolution makes it possible to exploit more efficiently the possibility, peculiar of DH, to focus on different object planes: thanks to the increased numerical aperture of the synthetic hologram, the depth of focus is decreased and it becomes possible to read the Augustus inscription on the base of the statue in the reconstructed image (left image of figure 3.11), or to focus on Augustus face (right image of figure 3.11), simply changing the numerical reconstruction distance.

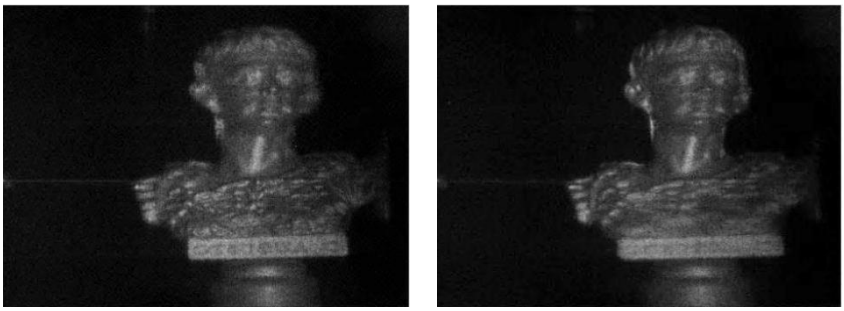

Figure 3.11: Stitched Augustus hologram amplitude reconstruction with Augustus inscription in focus (on the left) and with Augustus head in focus (on the right).

Figure 3.12: Perseus hologram stitching. (From left to right) Single hologram amplitude reconstruction; 4 × 3 stitched holograms amplitude reconstruction.

3.2.3 Human size holograms

As we have shown in chapter 2, by means of long wavelength DH, it is possible to obtain advantages in terms of larger field of view and lower seismic noise sensitivity. Furthermore, using a high power source like our CO_2 laser, it is possible to irradiate uniformly large surfaces. With long wavelenght radiation it becomes possible to record holograms in critical conditions including illuminated environments and not ground isolated setups in outdoor applications. Moreover, at this wavelength, holographic videos of moving objects, although with limited speed, can be easily recorded and reconstructed. All these features are fundamental if large sample

holograms are to be recorded. One of the peculiar difficulties in recording a large object digital hologram consists however in irradiating effectively the entire surface of the sample. In order to obtain optimal homogeneous sample irradiation we tested four different configurations and managed to record and reconstruct human size holograms [19] and, what is even more interesting, alive people holograms [32]. In order to compare the results obtained with each configuration, the object, a plastic mannequin 1.90cm high (figure 3.12), was maintained always in the same position with respect to the thermocamera. In particular, the distance between the object and the thermocamera was the minimum distance to record holograms of that size according to the equations discussed in chapter 1. The four setups shown below were just simple variations with respect to the basic configuration, differing from each other just in the way the sample was irradiated.

Single beam setup

The first configuration corresponded exactly to the base configuration except for the object beam lens L_1 which was substituted with a shorter (1inch) focal length lens in order to obtain a larger beam size across the sample. This configuration however suffered from important issues: since the peripheral part of the gaussian object beam is characterized by a lower intensity, the object surface was not uniformly irradiated and this reflected in a poor and inhomogeneous reconstruction quality of the outer part of the sample. Further, the object beam dimension was limited by the focusing power of the lens and, consequently, only a portion of the sample could be fruitfully irradiated. In these conditions we could not take complete advantage of the increased field of view offered by the longer wavelength because the irradiated area was smaller than the maximum recordable size.

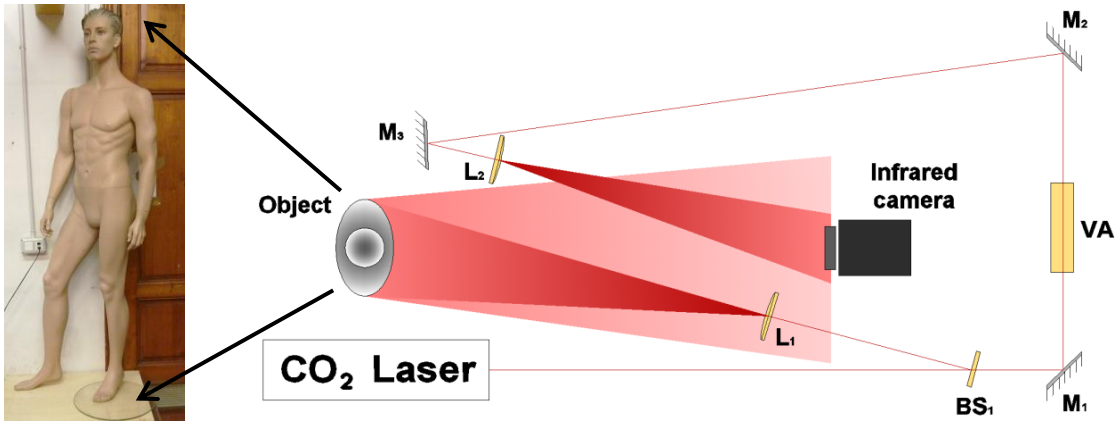

Figure 3.12: The object, a plastic mannequin 1.90cm high. Single beam setup. L1 is a ZnSe 1 inch focal length spherical lens.

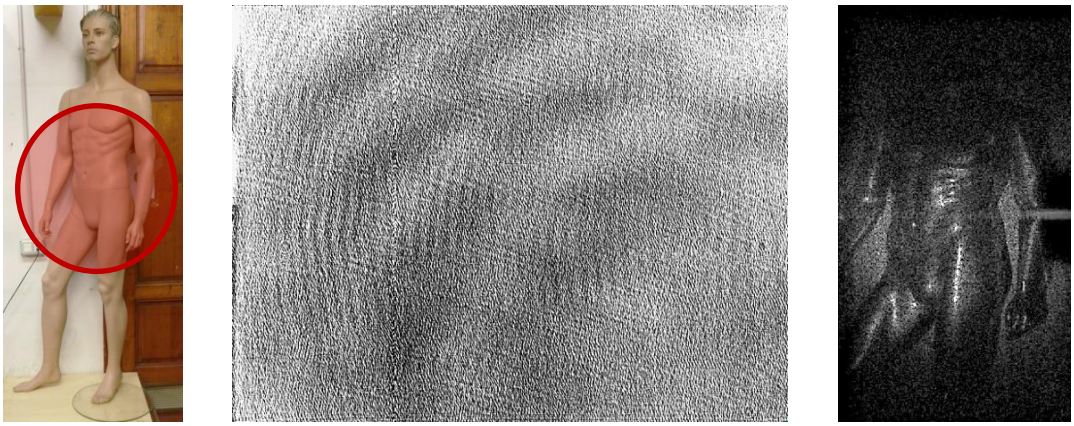

Figure 3.13: (From left to right) Mannequin image with irradiated area in red; mannequin hologram acquired with single beam setup; mannequin hologram amplitude reconstruction.

Double beam setup

A first solution to the inconveniences of the previous setup was obtained by means of the set up shown in figure 3.14. The object beam, after lens L1, was divided by means of a Zn Se 50/50 beam splitter, BS2, into two beams of equal intensity: the transmitted one was directed toward the lower portion of the sample, while the reflected one was directed toward the upper part of the sample by means of the plane mirror M4. Using this configuration we were able to irradiate almost completely the mannequin with a more uniform energy density. As shown in the numerical

reconstruction of figure 3.15, almost all the desired region was covered and the mannequin became nearly completely visible in the reconstruction image. Similarly to the previous configuration, however, in those regions of the sample where the beams were less intense or superimposed, the reconstruction became less clear.

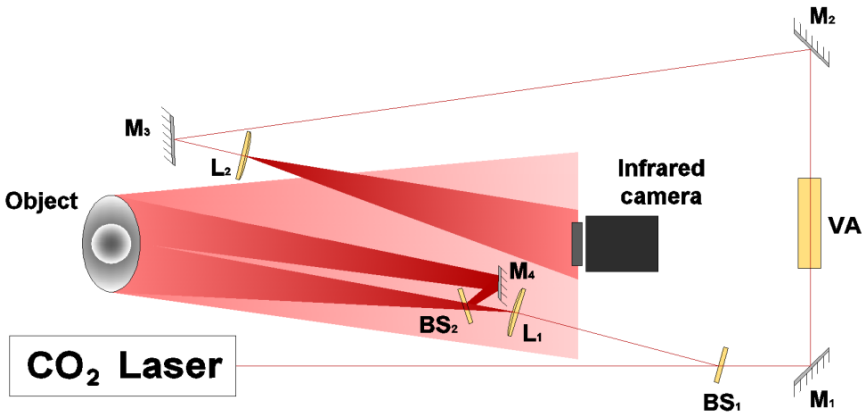

Figure 3.14: Double beam setup. M4 is a plane mirror, BS2 is 50/50 ZnSe beam splitter.

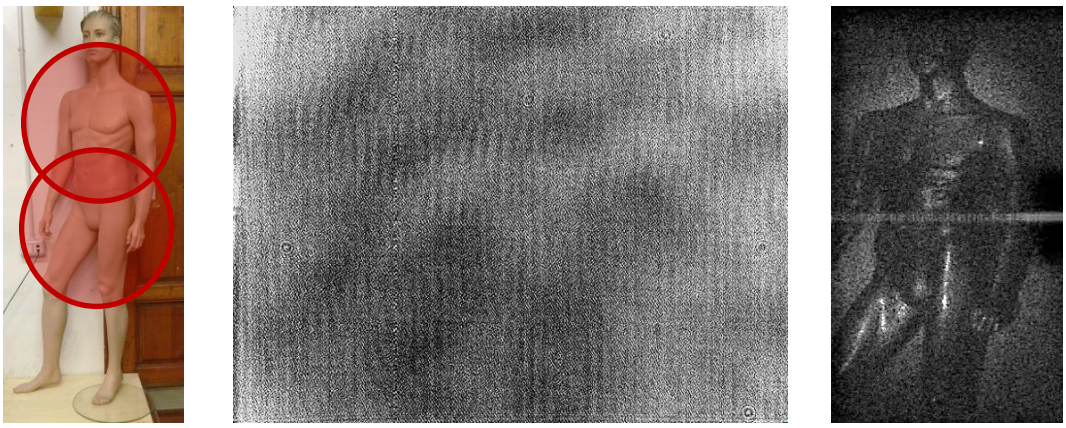

Figure 3.15: (From left to right) Mannequin image with irradiated area in red; mannequin hologram acquired with double beam setup; mannequin hologram amplitude reconstruction.

Cylindrical lens setup

In the third configuration a cylindrical lens was inserted just after the spherical one in order to obtain a stretched beam. This beam profile can be fruitfully employed when the analysis of samples with a preferential direction, like our mannequin, is

needed. Using the cylindrical lens it is possible to exploit more efficiently the available beam energy with evident advantage, as shown in figure 3.16.

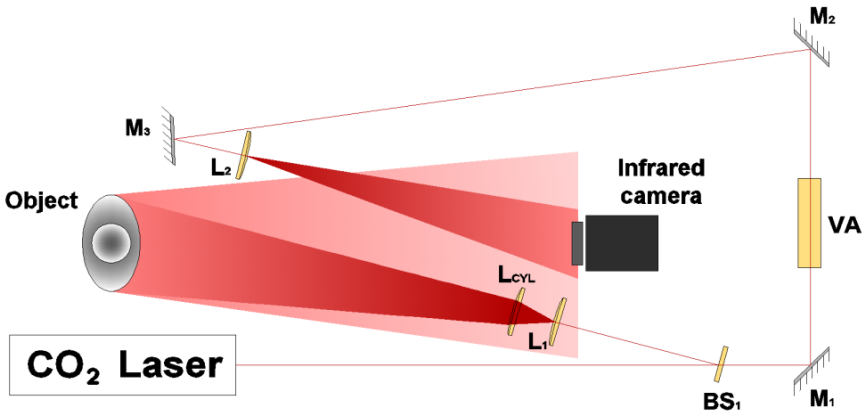

Figure 3.16: Cylindrical lens setup. L_{CYL} is a ZnSe 5cm focal length cylindrical lens.

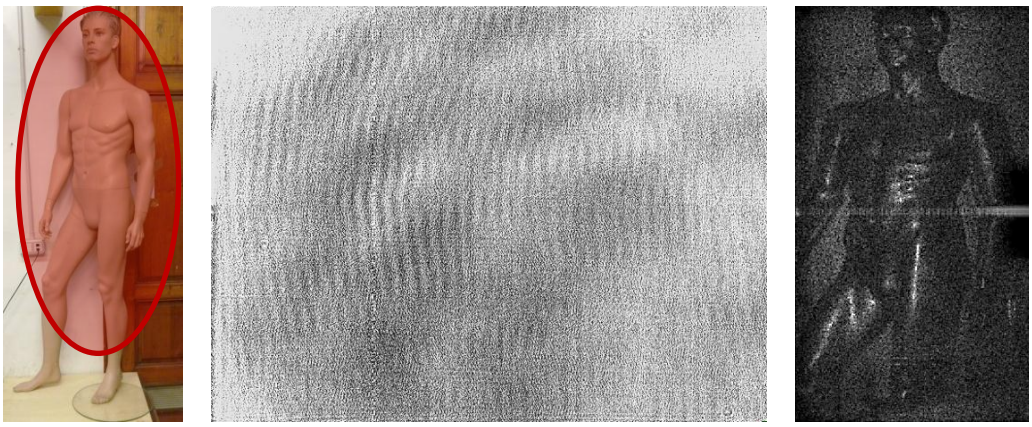

Figure 3.17: (From left to right) Mannequin image with irradiated area in red; mannequin hologram acquired with cylindrical lens setup; mannequin hologram amplitude reconstruction.

Scanning beam setup

The last configuration (figure 3.18) is based on a completely different approach. In this case we used a single object beam, expanded by the usual spherical lens L1, and moved it along the sample, changing its propagation direction by means of the plane mirror M5 driven by two motion control devices (NewStep NSC200 by Newport). Using this configuration we were able to uniformly irradiate, an overall surface of more than $4m^2$, an area larger than the admitted field of view. In this case

we recorded a video hologram during which the object beam scanned entirely the mannequin surface in about half a minute (video 3). When faster scanning acquisitions are realized the fringe visibility decreases progressively and the reconstruction resolution gradually reduces; again this problem could be solved by means of a higher frame rate and a shorter exposure time. Such kind of an acquisition procedure can be exploited in different ways: the video hologram can be reconstructed as a video which can be reproduced at normal velocity showing a slow scan of the sample, or it can be decimated and played at incremented speed so that the amplitude image of the whole object is perceived all at once; a third possibility consists in extracting the most significant frames and obtain the whole image by their superposition as shown in figure 3.19.

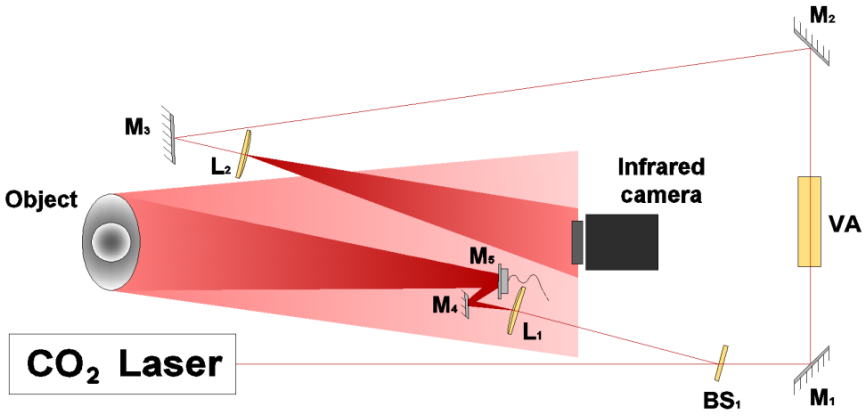

Figure 3.18: Scanning beam setup: M4 and M5 are plane mirrors driven by two motion controllers.

Figure 3.19: (From left to right) Mannequin image with irradiated area in red; mannequin hologram amplitude reconstruction at different scanning time and superposition of the most significant frames.

The natural following step was to test the possibility to acquire alive human being holograms [32]; using the first configuration we easily managed to acquire my half bust has shown in figure 3.20. Clearly, when operating with human beings, resolution get worse because of body micro movements and because of the lower reflectivity of human skin and clothes with respect to the plastic surface of the mannequin; it is, however, important to point out that such a result would be very difficult, if not impossible, to reach with a CW visible laser in not isolated conditions.

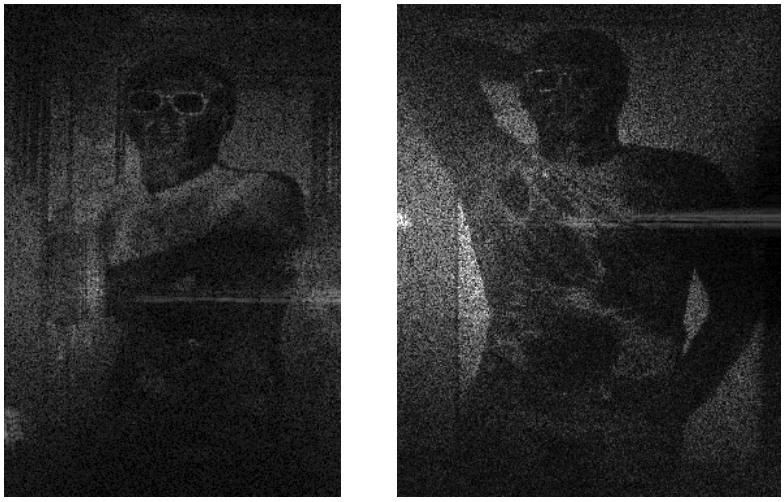

Figure 3.19: Amplitude reconstructions of my half bust with single beam setup.

Holography and, more generally, interferometry are commonly used for non-destructive testing of mechanical structures, stress analysis and quality control. The advent of DH has represented an invaluable advance in this field since it offered the possibility to perform real time investigations with a less expensive technique. A strong limit to this kind of application, especially for industrial purposes, is however represented by the presence of vibrations and by the limited sample dimensions admitted in visible DH. As we have demonstrated, IRDH, thanks to its capability to investigate large size samples without any particular attention to vibrations, represents thus a perfect candidate to substitute visible radiation for such purposes. Recently, also in the wake of the results obtained with our works, other research groups have developed such kind of non-destructive analysis by means of Mid IRDH [20]. With this technique it is in fact possible to follow, in real time, large samples deformations and quantify their amount evaluating the induced phase variation. In figure 3.20 a thermal expansion (due to laser heating itself) of Perseus statue has been revealed as phase variation with respect to the undisturbed initial sample condition (video 4).

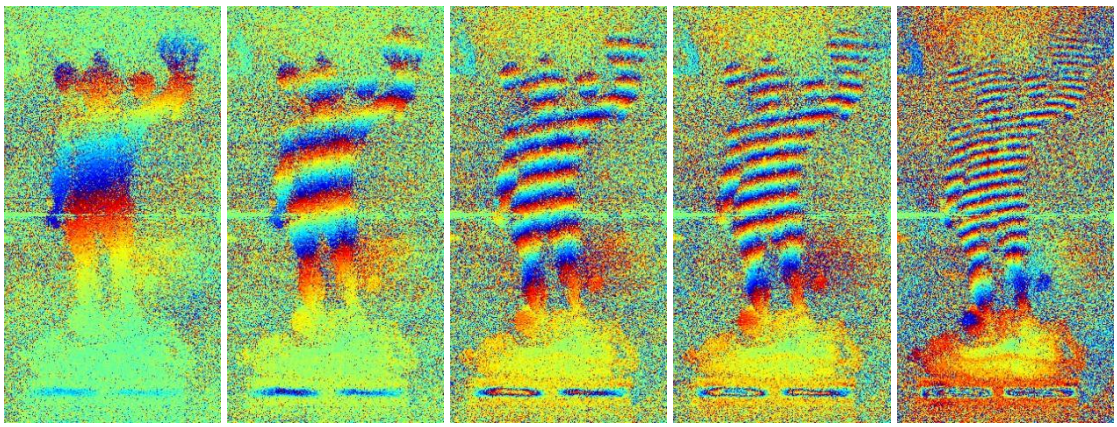

Figure 3.20: Reconstructed phase changes during Perseus statue heating with respect to the undisturbed initial condition.

3.2.4 Visible analog reconstruction of IR digital holograms

Holograms reconstruction in DH is usually implemented by means of numerical algorithms but nothing prevents to 'write', somehow, the hologram on an appropriate medium in order to perform an analog reconstruction. Spatial light modulators (SLM) (arrays of pixels where each pixel modulates the phase and the amplitude of the light transmitted through or reflected from it) are the elective devices to accomplish this particular task [39;62]. However, in general, the SLM pixel pitch d_{pSLM} differs from the digital hologram (recording device) pixel pitch d_p and this discrepancy may represent an important complication. Furthermore an optical reconstruction makes sense only if visible light is used while our holograms were recorded in the IR range. The so called *imaging equations* [47;21] relate the coordinate of an object point with that of the corresponding point in the reconstructed holographic image, in the most general conditions, that is for a rescaled hologram and for different recording/reconstruction wavelengths. According to these equations, the distance at which the reconstructed image appears in focus is [47;21]

$$z_{im} = \left[\frac{1}{z_{rec}} \pm \frac{\mu}{m^2}\left(\frac{1}{z_{ref}} - \frac{1}{z_{obj}}\right)\right]^{-1}$$

Where

z_{im} is the Z coordinate of the reconstructed object image,

z_{obj} is the object distance from the hologram plane,

z_{ref} and z_{rec} are the coordinates along the Z axis of the origin points of the spherical reference and reconstruction beams, respectively,

$m = \frac{d_{pSLM}}{d_p}$ is the scale change factor of the hologram,

$\mu = \frac{\lambda_2}{\lambda_1}$ and λ_1 and λ_2 are the recording and reconstruction wavelengths, respectively.

The upper set of signs applies for the one image wave and the lower set for the other. When z_{im} is negative, the image is virtual and lies to the left of the hologram, while when it is positive, the image is real and lies to the right of the hologram. Depending on the geometry it is possible for one image to be real and for the other to be virtual or for both to be real or both virtual.

Furthermore, according to the imaging equations, the reconstructed image undergoes a transverse magnification and longitudinal (or axial) magnification respectively equal to [47;21]

$$M_t = m\left(1 \mp \frac{m^2}{\mu}\frac{z_{obj}}{z_{rec}} - \frac{z_{obj}}{z_{ref}}\right)^{-1}, \quad M_l = \frac{1}{\mu}M_t^2$$

We note that, if the hologram is recorded in a lensless Fourier holography configuration $(z_{obj} = z_{ref})$,

$$z_{im} = z_{rec}$$

regardless of the wavelengths ratio and of the scale change factor of the hologram and the magnification factors simplify as follows

$$M_t = \mp\frac{\mu}{m}\left(\frac{z_{im}}{z_{obj}}\right), \quad M_l = \frac{\mu}{m^2}\left(\frac{z_{im}}{z_{obj}}\right)^2$$

Generally, therefore, when a 3d hologram reconstruction with a different wavelength is performed, the resulting image is affected by aberrations (spherical aberration, coma, astigmatism, field curvature and distortion). The expression of these various aberrations can be deduced from the imaging equations and it can be demonstrated [36] that lensless Fourier holography configuration minimizes most of them.

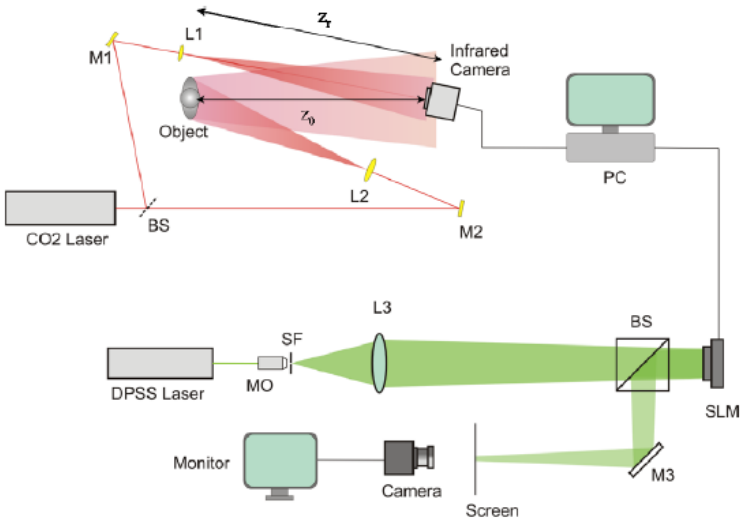

Figure 3.21: Experimental setup for recording-reconstruction process. M is a mirror, L is a lens, BS is a beam splitter, MO is a microscope objective, SLM is a spatial light modulator, SF is a spatial filter.

Single SLM

In a first work [42], 10.6μm holograms of the habitual Perseus statuette were recorded in the basic holographic arrangement but in a lensless Fourier holography configuration. In particular, we acquired 120 holograms rotating, each time, the figurine around itself of 3 degrees. In the reconstruction process, we used a diode pumped solid state laser emitting at 0.532μm. The laser beam was optically manipulated in such a way as to obtain a converging beam impinging on a reflective liquid crystal on silicon (LCoS) phase only SLM (PLUTO by Holoeye with 1920 × 1080 pixels, 8μm pixel pitch and 60 Hz frame rate) where the acquired holograms were played back in sequence with regular frequency (figure 3.21). With such an arrangement it was possible to obtain an analog reconstructed video of the rotating figurine on a screen at a fixed distance from the SLM (video 5). An image of the optically reconstructed wavefront, acquired by means of a standard CCD camera, is compared with a standard numerical reconstruction image in figure 3.22.

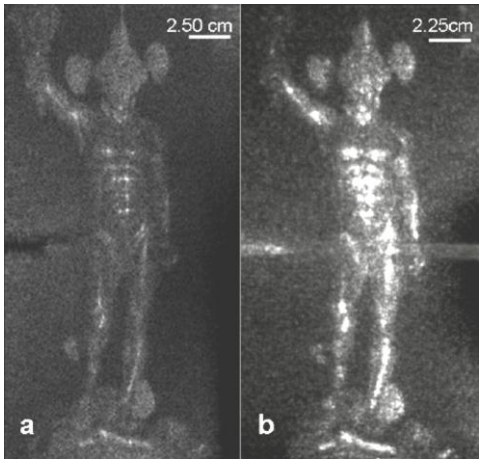

Figure 3.22: (a) Numerical reconstruction of Perseus statuette hologram (b) SLM optical reconstruction of Perseus statuette hologram performed at a visible wavelength and collected by a monochromatic CCD.

The experimental reconstructed image position and its magnification with respect to the real object, were in good agreement with the values predicted by the theoretical expressions and no significant aberration was observed. In order to verify that no aberration really affected the displayed image in our case, we inserted our experimental conditions values in the theoretical aberration coefficients expressions confirming that the wavefront aberrations were all negligible (< 1 wavelength) and did not substantially affect the reconstructed images.

Finally, by means of a numerical procedure [41], we created synthetic scenes that could be optically displayed. The procedure is based on recording several digital holograms of individual objects covering a 360° perspective. Each hologram is geometrically transformed to change the object's position and size within a very large depth of field and it is thus possible to create a dynamic 3D scene in which the object travels backwards and forwards in the 3D volume while performing a "pirouette". Combining holograms corresponding to different objects, it is also possible to create dynamic scenes with two or more objects rotating while travelling back and forth (figure 3.23).

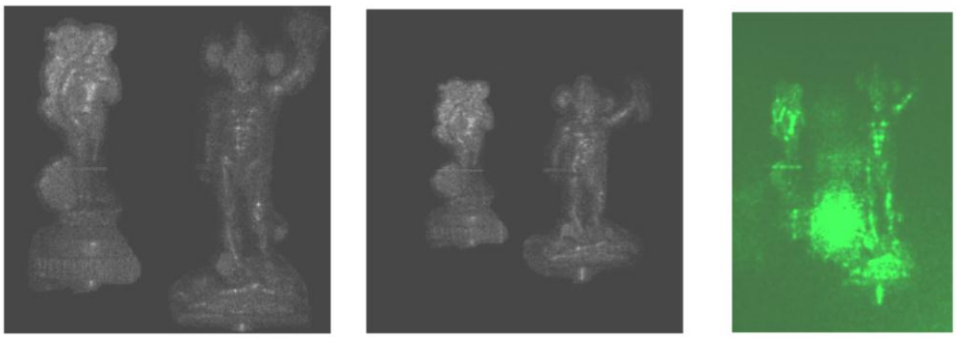

(a) (b) (c)

Figure 3.23: Numerical (a, b) and optical (c) reconstructions of the synthetic holograms obtained by combining the digital holograms of Perseus and the digital holograms of a similar statue representing Botticelli's Venus. The reconstruction distance is chosen in order to have Perseus and Venus in focus when they are close-up (a) or when they are far away (b).

Multiple SLMs

In a second work [50], in collaboration with the Department of Electrical and Electronics Engineering of Bilkent University (Turkey) and with the Bulgarian Academy of Sciences of Sofia (Bulgaria), we managed to obtain a holographic digital video display of a three-dimensional ghostlike image of Perseus multiview recorded holograms, floating in space. To achieve this result we used a holographic video display system built from nine LCoS phase only SLMs (Holoeye HEO-1080P with 1920×1080 pixels, $8\mu m$ pixel pitch and $60\,Hz$ frame rate) forming a circular configuration (figure 3.24). Elimination of the gaps between the SLMs was provided by a beam splitter to tile them side by side [61] and to achieve a virtual alignment with a continuous increased field of view. To position the reconstructed 3D image slightly above the display setup and to avoid blocking of the observer's vision by the display components, the SLMs were also tilted up at a small angle. Negligible reduction in the quality of the reconstructions for a tilted illumination of up to 20° has been shown by experiments [60]. All SLMs were illuminated with a single astigmatic expanding wave by means of a cone mirror as shown in figure 3.24. With the help of

this configuration observers can see 3D ghost-like image floating in space and can move and rotate around it (video 6).

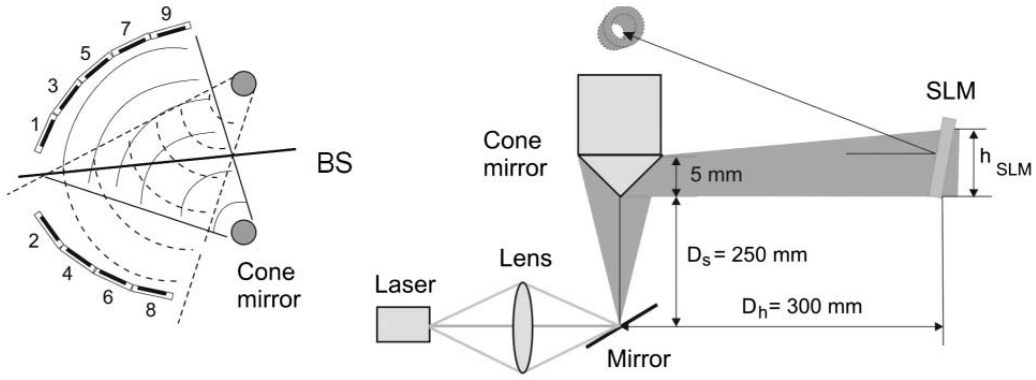

Figure 3.24: Circular holographic display. Left, arrangement of the nine phase-only SLMs, denoted as 1…9. Right, illumination of a single SLM.

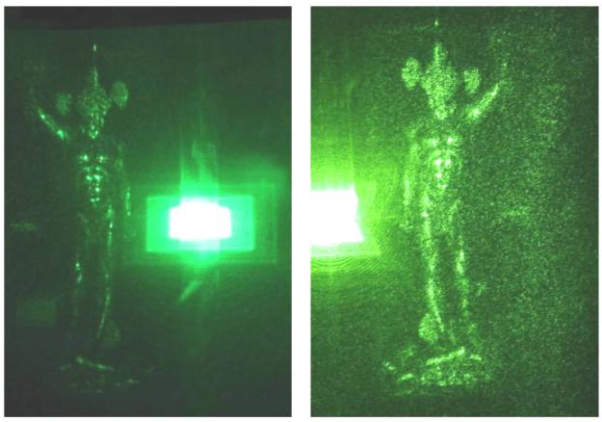

Figure 3.25: Left, single SLM optical reconstruction at 0.532 μm of the hologram captured at 10.6 μm and projected on a screen. Right, ghostlike multiple SLMs optical reconstruction of the same hologram.

These two works demonstrates the possibility of obtaining direct real time 3D vision of IR recorded digital holograms and, considered the previously underlined capability of IRDH to investigate large size samples, emphasize the potentialities of IRDH as valuable candidate in the research field of real 3d TV and for possible virtual museum applications.

3.2.5 Smoke and flames hidden object holograms

In this section we report our latest results in the field of IRDH at $10.6\mu m$; in particular we illustrate one more useful peculiarity of this technique, that is the possibility to detect object, or even animate beings, through smoke and, what is even more noticeable, through a wall of flames. The ability to monitor objects completely hidden, in the visible range, by smoke and flames and the even more interesting possibility to detect alive people in fire scenarios is a key and challenging target for its possible industrial applications and for its possible remarkable military and, above all, safety purposes. Visible radiation is strongly affected by smoke or fog and vision can be completely impaired in smoky environment. On the contrary last generation of uncooled IR microbolometer detectors, commercially available for imaging in the thermal infrared, allow passive or active (i.e. with IR laser illumination) clear vision through such scatterers since the IR electromagnetic radiation is just slightly scattered by fog drops and smoke particles. This property of IR radiation is well known and in fact many fire departments already use this kind of technologies for exploring fire scenarios in order to have a clearer vision and to operate safely in such hostile environments. Unfortunately, in presence of flames, even these detectors cannot be of great help since the electromagnetic radiation emitted by flames can severely saturate them, as well as standard CCD or CMOS, occluding the scene behind the flames.

As we have repeatedly stated, DH at long IR wavelength has considerable advantages, with respect to visible DH, that make it very flexible and useful for recording real world large scenes. Thanks to the longer wavelenght, IRDH is characterized by a lower seismic noise sensitivity and a larger field of view; as we have proved, these features allow to record digital holograms of large dynamical scenes and make it possible to obtain human moving holograms in CW conditions; the broad availability of high power CO2 laser sources with good coherence properties makes it possible to expand the object beam and achieve an efficient irradiation across very large scenes without too much restrictive limits on the optical path difference between object

beam and reference beam. Furthermore IR digital holograms can be recorded in open space and daylight conditions thus allowing this technology to be directly brought out of the laboratory. Another important characteristic to remember is the possibility to use only a portion of the acquired hologram to reconstruct the entire scene even if at the expenses of resolution. Finally DH usually employs a lensless setup to obtain out of focus acquisitions and to recover numerically, in the reconstruction step, the object wavefield at the desired focus plane.

All these features, combined with the possibility to exploit IRDH to see behind smoke and flames, which is, to our knowledge, not achievable by any other imaging technique, provides the unique possibility to perform real time dynamic detection of moving people in fire scenes. Indeed, as we have proved, IRDH allows not only to record objects immersed into smoke but also to visualize objects behind flames independently from the chemical nature of the involved burning materials and from their emission spectrum. On the contrary, we have verified how standard IR imaging cameras cannot carry out this task. In order to demonstrate these unique imaging potentialities, two kinds of experiments were conducted, where the capability of seeing through smoke and flames by IRDH were respectively tested.

Seeing through smoke

In a first series of experiments [32] we tested the capability of IRDH to work efficiently in smoky environments. In order to investigate this condition we used the basic holographic setup but immersed the object under investigation in a thick blanket of smoke (figure 3.26). As test object we used the habitual small Augustus statuette but, in order to obtain enough high smoke density around it, we put it inside a sealed Polymethyl methacrylate (PMMA) box. In one face of the box two windows in the infrared range where fixed: an input AR/AR ZnSe input window through which the laser beam could reach the object and a germanium output window through which the light diffused by the object could reach the thermocamera.

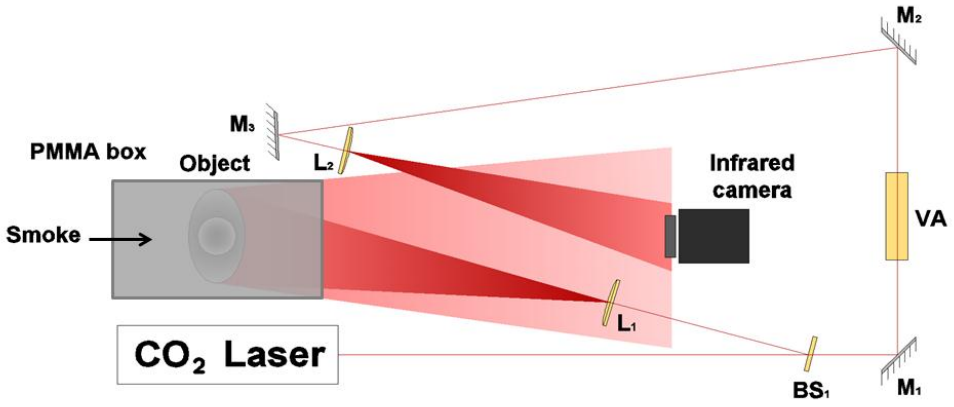

Figure 3.26: Imaging through smoke setup.

By means of a lateral aperture practiced in the box we let the smoke obtained by burning incense in a small furnace, enter into the box and, at the same time, we started acquiring a holographic video of the interferometric pattern with the increasing smoke density and a standard video in the visible range to testify the complete invisibility of the sample at the maximum smoke density (video 7). In order to have a quantitative measurement of the smoke concentration inside the box at any moment, we evaluated the intensity attenuation of a $15mW$ laser diode radiation travelling $6cm$ inside the box before reaching a silicon photodiode; by means of an HP 3401A multimeter we could check the current at the photodiode output so that the extinction coefficient at any smoke density could be evaluated by means of Lambert Beer law. In figure 3.27 the visible images of the empty box and after inletting smoke are shown; evidently at high smoke density the vision is completely impaired because of the severe scattering of the visible radiation; at the maximum smoke density the current in the photodiode was reduced by two orders of magnitude and it was impossible to see the statuette even from the short side of the box. In figure 3.27 the images obtained with the thermocamera working in normal mode with its IR objective in the two conditions are also shown. As expected, with a standard

thermographic image the object immersed in the smoke is still clearly visible since IR light at such long wavelength is only slightly scattered by smoke particles (according to Rayleigh and Mie scattering laws). Finally, the reconstructed IR holographic images in the two conditions, shown in figure 3.27, demonstrate that a clear vision through smoke can be obtained by means of IRDH too.

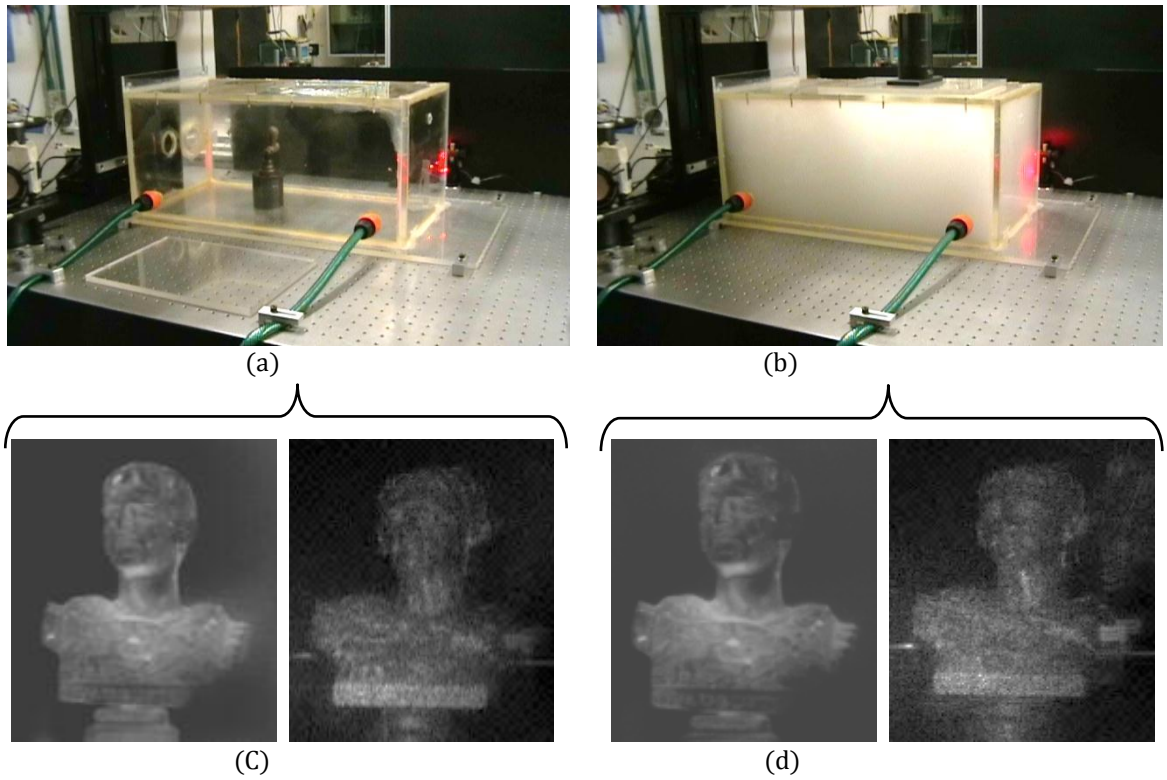

Figure 3.27: (a) Augustus statuette in the PMMA box without smoke. (b) Augustus statuette in the PMMA box with smoke. (c) PMMA box without smoke: thermographic imaging of Augustus on the left and hologram amplitude reconstruction on the right. (d) PMMA box with smoke: thermographic imaging of Augustus on the left and hologram amplitude reconstruction on the right.

It is important to note here that the random movements of the scattering particles (smoke and dust particles), which represents a noise source in the standard thermographic image, on the contrary may contribute to reinforce the clear vision in the holographic image: indeed we will show that, if multiple acquisitions are reconstructed and opportunely averaged, improved images with higher resolution can be obtained.

Seeing through flames

In a second series of experiments [32] we tested the capability of IRDH to detect an object hidden behind a curtain of flames. In order to investigate this possibility we used the basic holographic setup but inserted flames between the thermocamera and the object under investigation (figure 3.28).

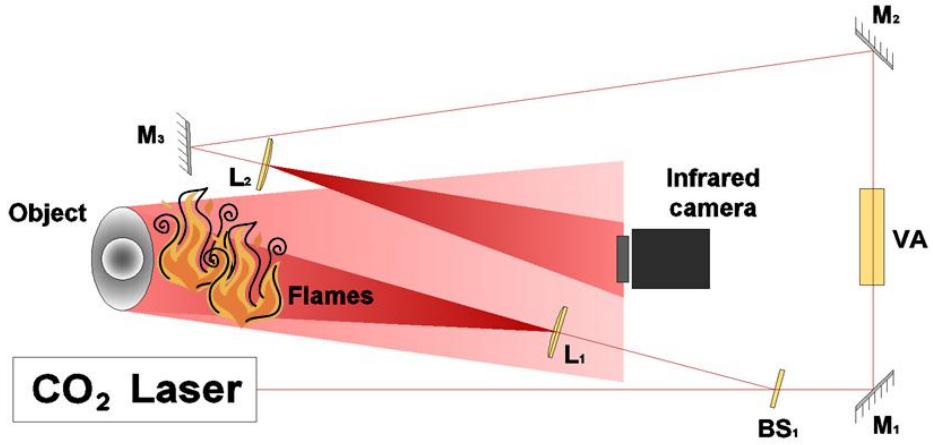

Figure 3.28: Imaging through flames setup.

The first tests were performed using as object the habitual Augustus statuette but then the setup was rearranged in order to test the technique with human beings. The flames were obtained employing candles in case of Augustus holograms and portable mini stoves for human size targets. In both cases a large portion of the object was covered by flames, impairing its vision to a normal CCD camera but also to the thermocamera. On the contrary, the holographic recorded images showed no such a problem, allowing to see through flames without significant resolution loss. This capability can be explained by the fundamental intrinsic features of holography. First of all, since no objective is required during holograms recording, the IR radiation energy emitted by the flames is not focused on the detector but is distributed over its

whole surface; this means that no image of the flames is formed on the detector and, consequently, no pixel saturation effect is obtained (figure 3.29). In other words, since out of focus images are recorded in DH, the typical saturation effect of the IR camera elements observed in standard imaging configurations is avoided and the sensor is not blinded by the flame emission. If the radiation energy intercepted by the sensor should be so high to disturb, somehow, the detector, it would be however always possible to use a narrow band filter around $10.6\mu m$ to completely remove its contribute.

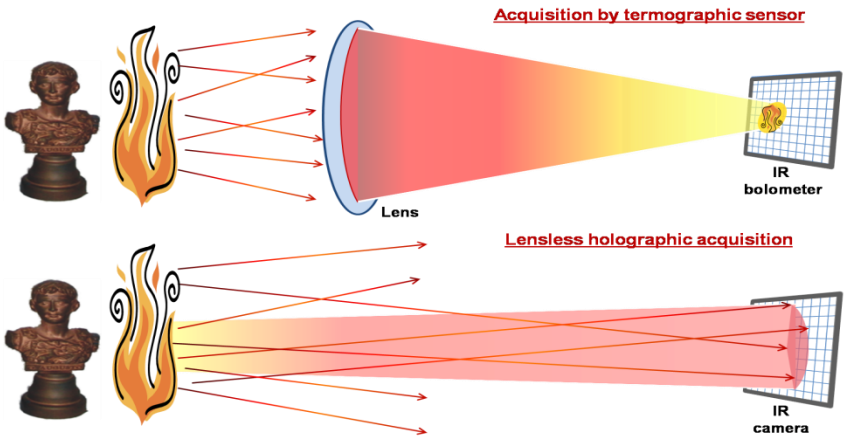

Figure 3.29: (Top) Detector saturation in presence of the thermocamera lens. (Bottom) Homogeneous background in the lensless holographic configuration.

A second important aspect of the question, strictly related to the interferometric character of DH, is that the flames radiation is not coherent with the radiation used to get the interferogram and consequently it does not affect the interferometric pattern in any way.

Furthermore, thanks to the ability of holography to reconstruct entirely the object wavefront from a smaller portion of the hologram, this technique allows an enhanced vision even if some macro-particles, often present in real fire-scenarios, obstruct direct imaging.

The only difficulty in recovering the object image with this technique could be represented by the refractive index changes due to flames gases vortices which may affect the object wavefront in the same way in which hot air vortices in front of an object would distort its image in the visible range; the complication could originate from an excessively fast changing rate of the refractive index and, consequently, of the wavefront, but, even in this case, this complication could be solved with a higher frame rate thermocamera and lower exposure times.

The advantages of digital holographic image system with respect to standard thermographic and visible recording systems are clearly appreciable from the comparisons of the visible, the thermal and the holographic reconstructed images of the samples in figures 3.30, 3.31 and 3.32.

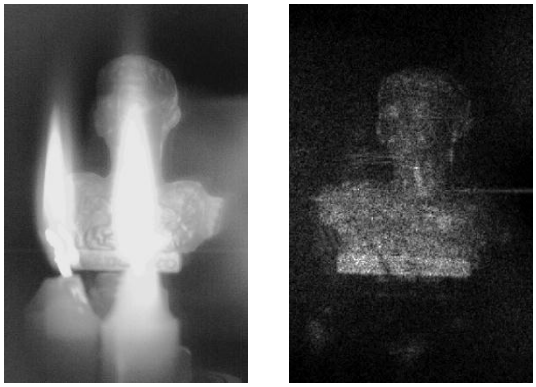

Figure 3.30: Imaging of Augustus statuette seen through candles flames. (Left) Thermographic image. (Right) Holographic reconstructed image.

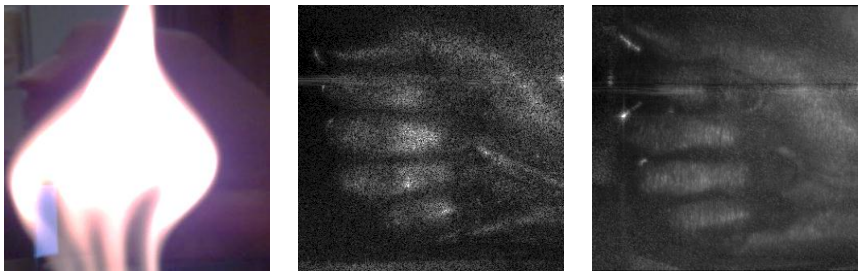

Figure 3.31: Imaging of a hand seen through stove flames. From left to right: visible image, holographic reconstructed image, enhanced holographic reconstructed image (see the end of the chapter for details on the enhancement procedure).

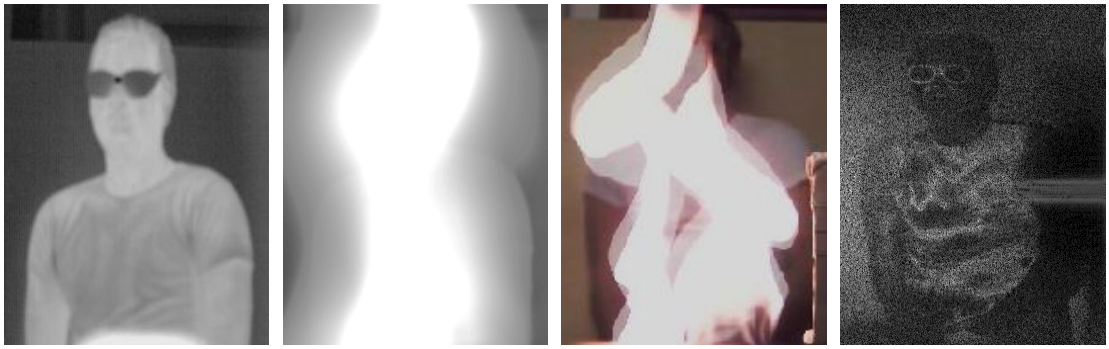

Figure 3.32: Imaging of an alive human being seen through two stoves flames. From left to right, thermographic image without flames, thermographic image with flames, visible image with flames, holographic reconstructed image with flames.

We hope that these experimental results could represent an important boost toward a detailed experimental analysis of the applicability of this technique in the industry and safety fields.

Speckle contrast reduction by multiple acquisitions

A further advantage of the proposed technique is that, through a numerical processing of the acquired holograms, it is possible to improve a posteriori the image quality reducing speckle noise. This feature could be exploited if, for example, it should be necessary an a posteriori analysis of the fire scene.

Speckle is a multiplicative noise which occurs whenever a coherent light hits on targets whose roughness varies on the same scale of the employed wavelength. In this case, each detector element records the coherent superposition of a number of different scattering contributions. As they experience microscopically different paths, their phases can be very variable and the result of the coherent superposition to the receiver is the typical succession of dark and bright spots known as speckle noise. As a result, the quality of the reconstructed hologram in DH gets worse in terms of contrast and pixel resolution. Due to the nature of the problem, it has been tackled in literature relying on statistical approaches. A common way to get indications about the speckle extent is to measure the speckle contrast as follows:

$$C = \frac{\sigma}{\mu}$$

where σ and μ respectively denote the standard deviation and the mean intensity of the image.

Furthermore, a punctual measurement of the intensity variations due to the speckle noise is obtainable by calculating the *relative deviation* as

$$R(x,y) = \frac{I(x,y) - \bar{I}}{\bar{I}}$$

Where $I(x,y)$ is the intensity of the pixel (x,y) of the reconstructed hologram and $\bar{I}$ its mean intensity calculated over the whole image. In particular, if a homogeneous portion of the original image is chosen, a smooth behaviour of the plot should be expected. So, any rapid variations and sudden spike in its shape have to be attributed to the speckle.

In order to reduce the speckle contrast it is possible to exploit some kind of diversity during holograms recording to obtain holograms from a set of uncorrelated speckle patterns and average them to get a multi-look (ML) image. Indeed, it can be shown [32] that the superposition of N statistically independent random variables returns a random variable whose variance is reduced of a factor $1/N$. Hence, the speckle contrast improves of a factor $1/\sqrt{N}$ with respect to the contrast of a single-look (SL) image.

Figure 3.32 shows the holographic reconstruction of Augustus statuette placed into the PMMA box of figure 3.26. In particular, we acquired a set of holograms after inletting smoke into the box, whose effect is to provide a temporal diversity. After a proper decimation of the original hologram stack we got a subset of $N = 25$ holograms and for each of them we performed the numerical propagation after dropping the diffraction orders out of interest. The reconstructed amplitudes have

been averaged and speckle measurements have been carried out on both the SL and the ML images in terms of the contrast estimators defined above.

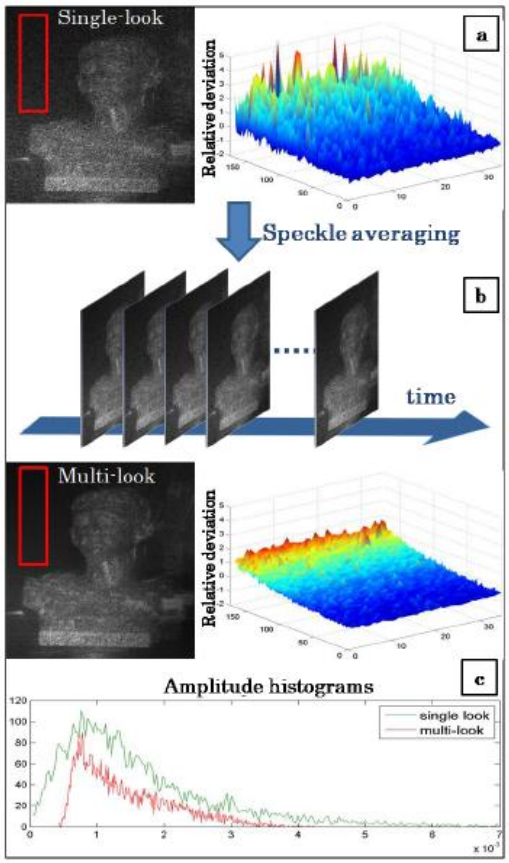

Figure 3.32: Imaging through smoke. (a) Holographic amplitude reconstruction before numerical processing and Relative Deviation corresponding to a homogeneous portion of the image (red box in figure). (b) Speckle reduction by processing a time sequence of holograms: multi-look reconstruction and Relative Deviation improvement. (c) Amplitude histograms: comparison between the single look and the multi-look image.

Figure 3.32 (a) shows the SL image and the relative deviation calculated over the homogeneous area corresponding to the red box in figure. As expected, the noise is responsible for the rapid fluctuations of $R(x, y)$ and the degradation due to speckle noise is evident in the amplitude image as well. In figure 3.32 (b) the described procedure is sketched and the resulting ML output is shown. The ML improvement is clearly appreciable in the amplitude image and the relative deviation exhibits a much

smoother behaviour. This suggests that a significant gain has been achieved in reducing the speckle noise by combining multiple acquisitions. This claim is confirmed by the measure of speckle contrast, which gets reduced of the 12% with respect to the SL image. However, a residual correlation between the employed frames is present, which in turn results in the gap with respect to the maximum theoretical improvement factor, i.e. the 20% in case of $N = 25$. As a further validation, we calculated the amplitude histograms in a homogeneous test area of both the SL and the ML reconstructions. As expected in the ML gain traduces in a smaller variance, which is apparent in the plots shown in figure 3.32 (c).

In case the line of sight between the target and the recording device is impaired by the presence of a flame, the gas vortices provide in turn a temporal diversity and a set of uncorrelated holograms can be acquired and temporally averaged to get again an improved ML output. Figure 3.33 shows the improvement achievable by numerical processing. In particular, in the SL image the effect of the saturation is apparent, with dark areas hindering a clear vision of the human target behind the flames; the human target becomes clearly visible in the ML reconstruction. In this way more details can be appreciated and a post analysis of the room scene is possible.

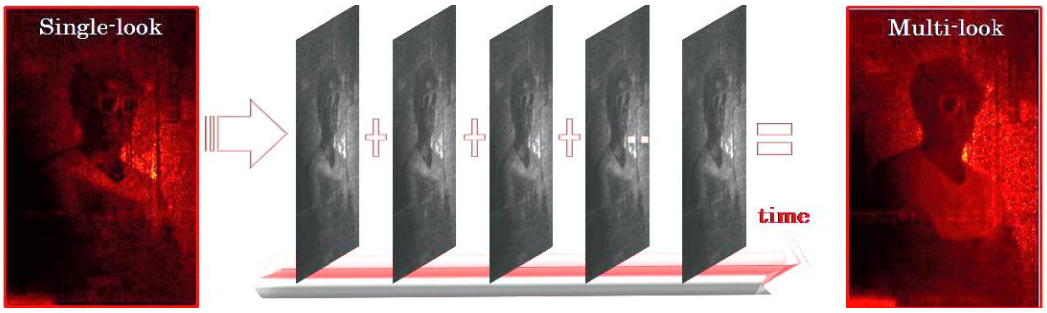

Figure 3.33: Imaging of a human target behind a flame. Left, SL holographic reconstruction. Right, ML holographic amplitude image.

4 Experiments with Terahertz imaging

The Terahertz frequency range has historically been characterized by a relative lack of convenient radiation sources, detectors and transmission technology and, for this reason, it has remained one of the least developed spectral regions. Over the last few years, however, THz radiation has become of large interest for its peculiar sensitivity to many molecular absorption lines, appealing for spectroscopic, astrophysics and biological analysis, and for its potential in non-invasive imaging applications, spanning from medical diagnostics to homeland security. This renewed interest has benefited particularly of the invention of Quantum Cascade lasers (QCLs) in 1994 [15] as well as of the recent development of electronic emitters, such as resonant tunnelling diodes, and frequency multipliers [51]. In comparison with visible or near infrared waves, THz radiation can penetrate organic materials such as plastics, clothes, wood, paper products and thin biological samples. Similarly to X rays, THz radiation cannot penetrate metals but differently from them, it is a not-ionizing radiation and, thanks to its low photon energy, it does not cause damage to the investigated materials. Thanks to such peculiar properties, THz radiation can thus be fruitfully employed for security screening and illicit material detection (safe body scanners, packaging inspection), non-destructive testing and quality control. Since the onset of THz imaging, in 1995, by Hu and Nuss [24], who coined the term T-rays, various imaging modalities for numerous applications have been proposed, developed and demonstrated. At the beginning the majority of research systems in THz imaging made use of Time Domain Spectroscopy (TDS) but several other configurations, including time of flight imaging [37], tomographic imaging [57], real time array detectors imaging [30;59], near-field sub wavelenght resolution imaging [7;8], have been successfully applied so far.

The second part of this PhD project has been devoted to this continuously developing and promising field of THz imaging. In particular we developed a simple

transmission imaging configuration which worked as starting point toward the almost unexplored field of THz digital holography.

4.1 Experimental apparatus

In all the experiments performed in the Far IR we employed the coherent radiation emitted by a Quantum Cascade Laser (QCL) processed at the Nanoscience Institute of Pisa (CNR); in particular the source at our disposal was a bound to continuum [54] QCL emitting at 2.8THz (111μm) driven in pulsed regime. The laser could operate up to 85 K and, consequently, a cryostat chamber (Ricor LV FA Cool) and a vacuum pump (Pfeiffer Vacuum Hicube TC110), to create vacuum in the cryostat chamber, were employed. A waveform generator (Agilent 33250A) combined with a current driver (Wavelength Electronics QCL 1000, 0.2 A/V transfer function) were used to drive the laser with the desired pulse duration. In graph 4.1 the QCL power vs current characteristic (5Hz square wave driving current with 50% duty cycle at $T = 20K$) is illustrated. As shown in the graph, in this operating conditions, the laser threshold is reached at about 0.6A and the maximum laser power (about 1.5mW) is obtained at about 0.9A of driving current.

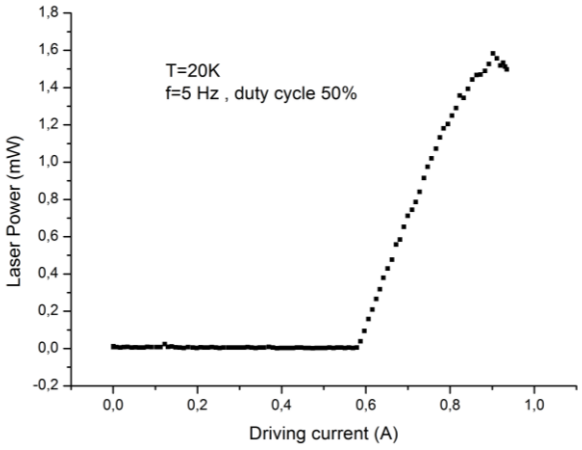

Graph 4.1: Laser output power vs laser driving current.

To detect laser radiation we had available in the laboratory different detectors:

- Pyroelectric array detector Pyrocam III by Spiricon (124×124 $LiTaO_3$ elements, pixel size $85\mu m \times 85\mu m$, centre to centre spacing $100\mu m \times 100\mu m$, Noise Equivalent Power $2.2mW/cm^2$ @ $24Hz$).
- Pyroelectric point detector Spectrum SPH 62 THz - Gentec QS2 THz BL (Effective aperture $2mm \times 2mm$, Noise Equivalent Power $4.0 \cdot 10^{-10}\, W/\sqrt{Hz}$, Voltage Responsivity $140KV/W$ @ $630nm$ $5Hz$).
- Pyroelectric point detector Spectrum SPH 31 THz - Gentec QS5 THz MT (Effective aperture $5mm$ ∅, Noise Equivalent Power $1.0 \cdot 10^{-9}\, W/\sqrt{Hz}$, Voltage Responsivity $70KV/W$ @ $630nm$ $5Hz$).
- Nanowires detectors (see nanowires paragraph for detailed description).

THz radiation is not transmitted through glass and, consequently, special optics are required; among the various materials currently employed to build THz optics, we had at our disposal some Polytetrafluoroethylene (PTFE or Teflon) lenses (quite inexpensive and simple to work material with, however, relatively low transmittance coefficient) and various Polymethylpentene (TPX) lenses and windows (more expensive material with higher transmittance coefficient both in the THz and in the visible range); however, when possible, we decided to use off axis parabolic (OAP) mirrors in order to reduce at maximum the beam attenuation.

4.2 Experimental setups and results

Considered the low sensitivity of the array detector at our disposal (Pyrocam III) and the limited output power of our QCL, it was not possible to detect collimated beams of lateral size comparable to the sensor dimensions and, consequently, use of the camera was restricted to focused beam detection and analysis. These detection restrictions prevented us from realizing a real time imaging system and forced us to implement a single detector system in which the whole sample surface could be

investigated by means of a motorized scanning system. This kind of imaging configuration has been widely employed so far in the THz range due to shortage of commercial detector arrays and, despite its low image acquisition rate, represented a convenient solution to test the newly conceived kind of sensors, based on field effect transistor nanowires, provided to our laboratory by the Nanoscience Institute of Pisa.
The realization of a DH setup without a sufficiently sensitive array detector was an even more challenging task. Single detector recording of an interference pattern, even if possible in principle [23], would be very critical because of fringe instabilities during the scanning process and would require smaller detector elements than ours, in order to sample correctly the narrow fringes required in off axis DH. The purchase of a higher sensitivity array detector was therefore an inevitable decision and a microbolometric focal plane array revealed to be the best choice; considered that high performance detectors of this kind are not yet widespread, the order required, besides great attention and economic effort, long times and it is currently still under processing.

4.2.1 THz imaging with single point detector

In figure 4.1 the scheme of the THz imaging setup realized in our laboratory is illustrated. We opted for a transmission configuration which could point out THz radiation penetration capability.
The QCL was indium soldered to a copper carrier mounted in the cryorefrigerator where vacuum and low temperatures were obtained. Due to the high angular divergence of the emitted beam, the device was placed as close as possible to the $2mm$ TPX cryorefrigerator window. In this configuration the laser diverging output was collimated by means of a first f/1 OAP mirror with $50.8mm$ reflective focal length (RFL). The collimated beam was then focused on the sample by means of a second f/1 OAP mirror with the same RFL. The sample was fixed, by means of a 'home made' sample holder frame to two motorized translational stages (LTS300 by Thorlabs) which could move the sample along the laser beam focus plane. The diverging beam

coming out from the sample plane was collimated by means of a third f/1 OAP mirror with the same RFL of the previous ones. The beam was finally focused on a point detector with a fourth, and last, f/1 OAP mirror with 38.1mm RFL. It should be remarked that this configuration made no use of lenses and the beam path had quite contained dimensions in order to reduce at maximum the atmospheric attenuation. The motorized stages were remotely controlled by means of a 'home made' Labview routine so as to obtain a raster scanning of the sample in front of the laser beam waist. The attenuated transmitted beam intensity was collected by the point detector so that image data were acquired one pixel at a time and the assembled image of the sample could be recovered at a later stage. Both pyroelectric detectors at our disposal and the Pyrocam were used to achieve an optimal alignment. A lock in amplifier (EG&G Instruments 7265 DSP Lock in Amplifier) was used to acquire the point detector response with an improved signal to noise ratio.

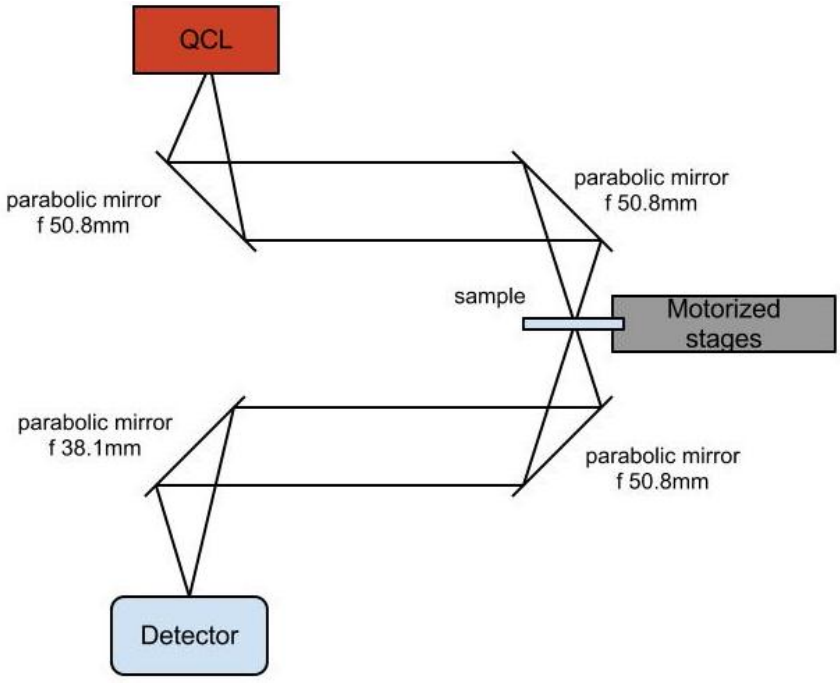

Figure 4.1: Terahertz imaging setup.

Acquiring with a pyroelectric sensor

In a first series of measurement, we used, as a point detector, the pyroelectric sensor Gentec QS2 THz BL. Working with pyroelectric detectors requires to low-frequency modulate the laser beam, e.g. by using a chopper or by modulating laser driving current. We opted for the second choice by combining the laser driving pulses ($20\mu s$, at a repetition rate of $10kHz$) with a 50% duty cycle square wave at $100Hz$. The detector signal was acquired by means of the lock in amplifier with a time constant of $20ms$ and stored in a *.txt file by means of the same Labview routine controlling the motorized stages. One of the two motorized stages scanned back and forth the sample surface in front of the focused beam with a fixed speed along the horizontal direction while the lock-in acquired the detector signal at a given rate; at each line end the other stage shifted the sample in the vertical direction of a fixed quantity. The horizontal and vertical pixel pitches of the final image were thus determined, respectively, by the fixed value of the vertical step and by the ratio between the horizontal scanning speed and the acquisition rate.

In order to have an estimation of the beam waist symmetry and dimensions in the object focus plane, we used, as a first sample, a $250\mu m$ pinhole and moved it in front of the beam focus with $20\mu m$ resolution in both directions covering a $1mm \times 1mm$ surface (graph 4.2). Since the pinhole diameter and the laser beam waist had comparable dimensions this method could only give an overestimation of the real beam characteristics. The two beam profiles resulted, however, to be quite symmetrical and the beam diameter was in good agreement with the expected value calculated on the basis of the laser divergence and of the OAP mirror RFL.

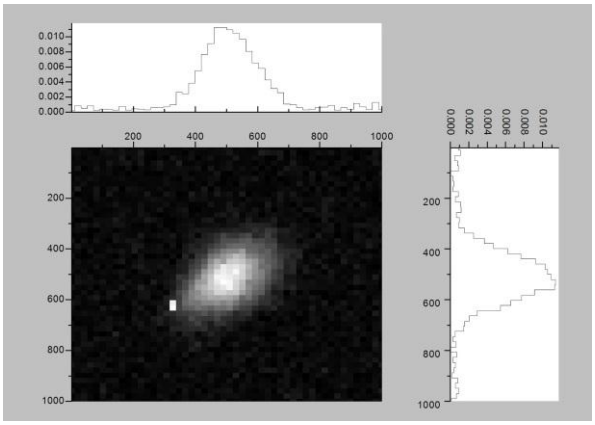

Graph 4.2: Beam waist image.

In order to test the resolution of our imaging system we acquired the image of an USAF Target (R74). In this first image (figure 4.2), acquired with a pixel pitch of about $100\mu m \times 100\mu m$, we managed to solve lines belonging to group 1 element 4, meaning a resolution of $2.828\, cycles/mm$ (about $177\mu m$) comparable to the diffraction limited resolution. The unexpected black spots inside some of the target slits are acquisition artefacts due to unwanted lock in saturation.

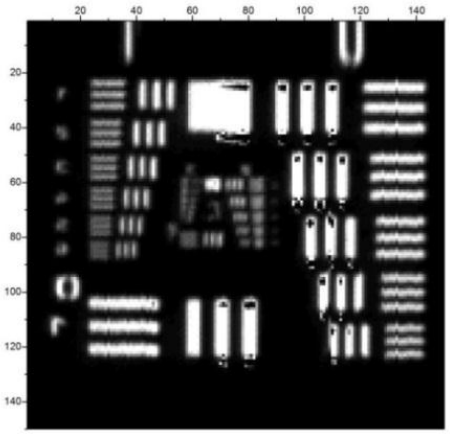

Figure 4.2: USAF target THz image.

We then decided to test our imaging system with a typical sample used in Terahertz imaging experiments [38], that is a partially dry leaf. The image, acquired with a pixel

pitch of about $100\mu m \times 100\mu m$, shown in figure 4.3, points out the ability of terahertz radiation to pass through opaque organic materials and to highlight their water content distribution; imaging with THZ radiation can therefore emphasize the vascular bundle system and the internal structure of the leaf.

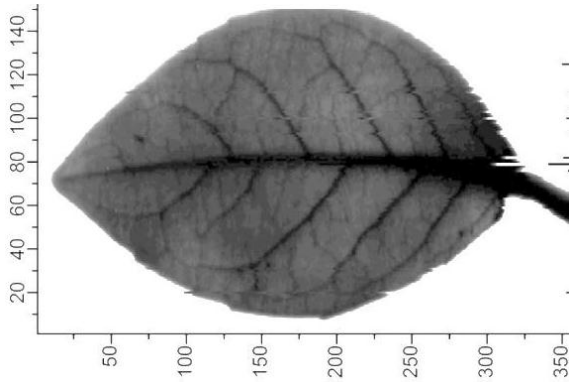

Figure 4.3: Dry leaf THz image.

This kind of setup can be easily employed in cultural heritage applications as is the case, for example, of certain pigments used in painting that are transparent at this wavelength, thus allowing the reconstruction of the underlying structures. It is thus possible to highlight fractures or detachments in the supporting layers of the pictorial work when paints on wood or frescos on masonry surfaces are investigated. With our configuration, in particular, we proved the capacity of 2.8 THz radiation to penetrate the white lead pigment, $(PbCO_3)_2 \cdot Pb(OH)_2$, commonly called *biacca*; this pigment, besides being employed as white painting colour, was sometimes used, even by important artists like Michelangelo Buonarroti, to cover pre-existing undesired drawings where new drawings were to be realized. We also tested the capacity of our system to detect iron gall ink or graphite letters written in old paper (figure 4.4). With a simple imaging system in the THz range, like the one developed in our laboratory, it would thus be possible to bring to light graphite or ink drawing or writings intentionally hidden by the artist under a white lead layer.

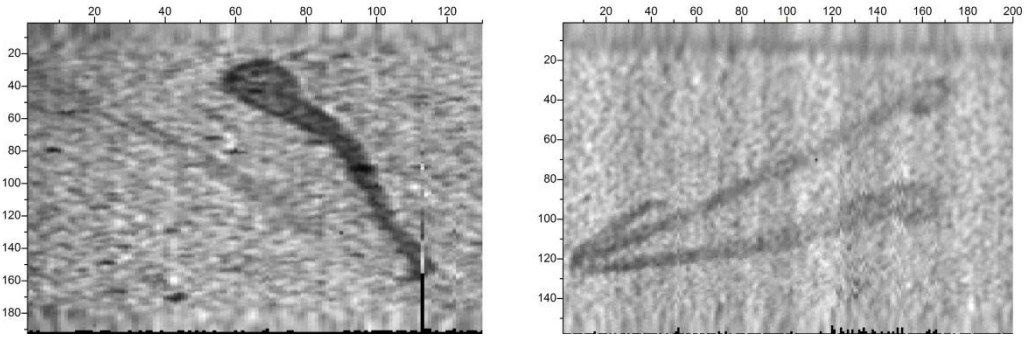

Figure 4.4: (Left) Iron gall ink "A" letter. (Right) Graphite "A" letter.

Acquiring with a nanowire sensor

In a second session of measurements we had the opportunity to test a new kind of THz detectors as point detectors for our imaging system: *nanowire detectors*.

Many THz detection system approaches have been developed so far, but a miniaturized room-temperature detector technology, which could be also easily integrated in an array configuration, is still largely missing. Semiconducting bolometers and hot-electron bolometers can be indeed conveniently coupled with QCLs leading to high signal to noise ratio but at the cost of a deep cryogenic cooling and, usually, a low dynamic range. On the other hand, room temperature THz detectors, such as pyroelectric detectors, Golay cells, and Schottky diodes, are either not very sensitive, or extremely slow, or operate well only at IR frequencies lower than $1THz$, therefore being not ideal for QCL sources. Commercial THz focal plane arrays, currently based on microbolometric elements, can be efficiently coupled with QCLs and have allowed demonstrating real-time imaging [30;59], but, presently, provide only moderate sensitivities and response speed. Schottky diodes, the prototypical electronic components for room temperature detection of high frequency radiation, exploit the nonlinearity and asymmetry of their current-voltage characteristic, to generate, through rectification, a continuous signal out of the oscillating incident electromagnetic field; this simple operating principle, however, has several drawbacks, related to the RC time constant, limiting the bandwidth

around 1THz and to the limited sensitivity. Considered the large interest in THz imaging applications, the development of a new solid-state technology for fast, room-temperature, terahertz detectors integrated in high-speed multi pixel arrays is highly desired. A possible route toward such a kind of detectors could be represented by nanostructure devices which, today, are at the forefront of studies on future electronics; the growth of semiconductor nanowires (NWs), in particular, has recently opened new paths to silicon integration of device families such as light-emitting diodes, high-efficiency photovoltaic devices, or high-responsivity photodetectors. NWs can be easily removed from the host substrate and placed on top of a new functional one for individual contacting, even in relatively large numbers, with a simple planar technology suitable for low-capacitance circuits. Therefore, in principle, they represent an ideal building block for implementing wave detectors that could be well operated into the terahertz, thanks to their typical attofarad-order capacitance. Recently, such a novel approach for the development of THz detectors by appropriately integrating conventional THZ detection geometries with nanowires structures has been proposed [53;55]. Specifically, semiconductor InAs nanowires grown bottom-up by catalytic process through vapour-phase epitaxy has been used as active element for the development of THZ detectors based on a FET configuration. The detection mechanism exploits the nonlinearity of the transfer characteristics: the terahertz radiation field is fed at the gate-source electrodes through wide band antennas, and the rectified signal is then read at the output in the form of a DC drain voltage. The terahertz detection principle in a FET was first explained by the Dyakonov-Shur plasma wave theory [13]. When terahertz radiation is coupled to the FET, between gate and source terminals, the ac terahertz voltage modulates simultaneously the carrier density and the carrier drift velocity. As a result, the terahertz signal is rectified and leads to a DC signal ΔV between source and drain terminals proportional to the received power. The value of this voltage (or current, depending on the read-out circuit) depends on the carrier density in the channel, which may be controlled by the gate voltage. The device operates as a square

law detector in which the largest non-linearity, leading to the highest responsivity, is achieved around the channel pinch-off. In addition, some asymmetry between source and drain is needed to induce ΔV; this can originate from the difference in the source and drain boundary conditions due to some parasitic capacitance, but usually stems from the asymmetry in feeding the incoming radiation, which can be achieved either by using a special antenna or by an asymmetric design of source and drain contact pads. Finally, the asymmetry can naturally arise if a dc current is passed between source and drain, creating a depletion of the electron density on the drain side of the channel. In particular, to increase the asymmetry, and therefore the responsivity, of the nanowire detectors provided to our laboratory, low shunt-capacitance antennas to funnel the radiation into the strongly sub wavelength detecting elements, were designed as contact pads. Antenna coupling ensures selective responsivity to both the spatial mode and the polarization of the incoming radiation. These very sensitive sensors, as every FET device, are quite delicate and need particularly careful handling especially from the point of view of accidental electrostatic discharges.

Following the standard characterization procedures performed in the papers describing these devices, we decided to test the electrical and responsivity properties of these nanowires. By means of X, Y, Z micro movements stages, we positioned the nanowire detector in the first focus of the beam path, where higher power was attained. We drove the laser with a $5.04 kHz$ and 30% duty cycle square wave current with amplitude of $0.75 A$ at a temperature of $25 K$ (when working with NWs bursting is no longer required). By means of the stages we positioned the NW so as to optimize the radiation-antenna matching and obtained a maximum signal of $350 \mu V$ at the drain electrode while applying a $7 V$ DC voltage to the gate terminal. The signal was then amplified 10X and sent to a real time signal analyser (Tektronix RSA 51106A) so that we could extract the power spectral density in a $200 Hz$ window and with $1 Hz$ of resolution bandwidth in three different conditions: laser on, laser off, laser on but blocked beam. As shown in graph 4.3 we had about 77db/Hz of SNR even if a portion

of the signal at the working frequency was probably coming from the laser electronic circuits.

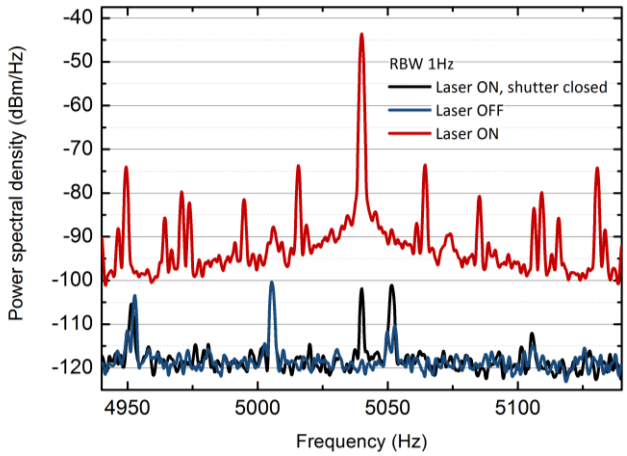

Graph 4.3: Power density spectrum of the signal with laser on (red), with laser off (blue) and with laser on but blocked beam (black).

We then acquired the frequency response of the detector in a broader frequency window (graph 4.4) gradually changing the frequency of the laser driving current.

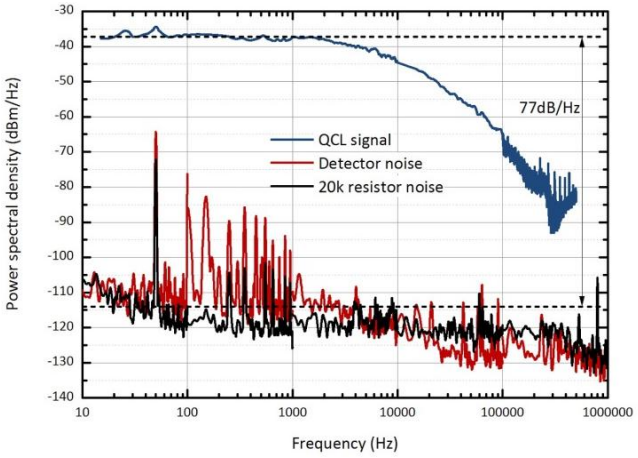

Graph 4.4: (Blue) Nanowire frequency response. (Red) Power spectral density of the detector noise. (Black) Power spectral density of a $20k\Omega$ resistor.

In the same graph it is also represented the power spectral density of the detector noise and the power spectral density of the Johnson noise at the terminals of a $20k\Omega$ resistor in the same frequency bandwidth. Coherently with the results presented in [55], the frequency response of the detector remained constant within $3db$ up to about $5kHz$. In this frequency region the detector noise spectrum seemed to be centered around about $115dbm/Hz$ as if the detector resistance were of the order of $120k\Omega$.

We then focused our attention to the detector response behaviour for different gate voltage values. To investigate this relation we used a waveform generator to apply a triangular wave at $1.4Hz$ going from $-8V$ up to $8V$ to the gate terminal. As shown in graph 4.5, the maximum nanowire response was obtained for a positive value of the gate potential V_g (about $6V$) but the curve showed clear hysteresis behaviour as confirmed in [53;55].

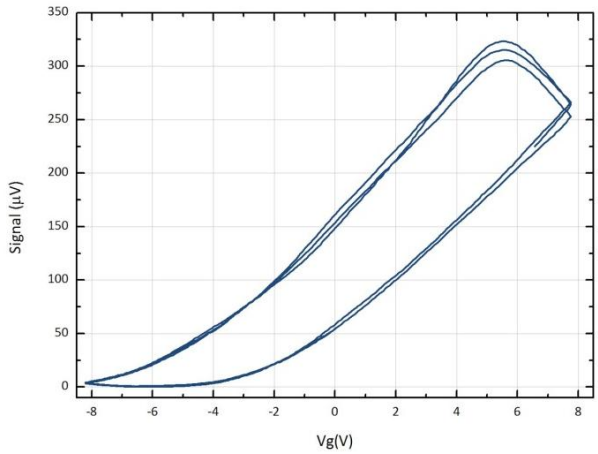

Graph 4.5:.Nanowire signal vs gate potential.

In the last characterization experiment we measured the source-drain I-V characteristics and recovered the resistance of the source-drain channel for different values of V_g. To perform this measurement we applied a constant voltage to the drain

terminal in series with a $5M\Omega$ resistor, and measured the current intensity at the output of the source terminal by means of a current amplifier converting the current into a voltage signal with an amplification factor of $10^6\,V/A$. The latter signal was sent to the oscilloscope together with the triangular wave at $10mHz$ going from $-8V$ up to $8V$ applied to the gate terminal. The results are illustrated in graphs 4.6 and 4.7.

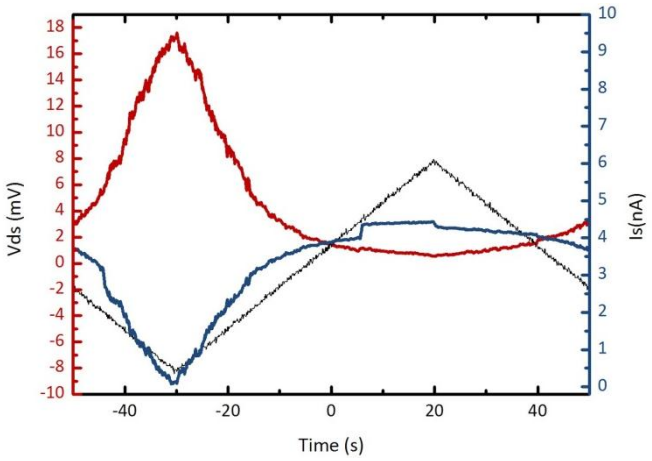

Graph 4.6: Source-drain I-V characteristic.

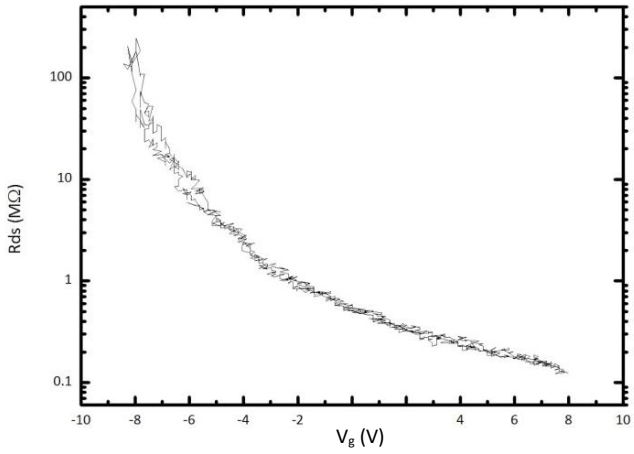

Graph 4.7: Source-drain channel resistance R_{ds} vs gate voltage V_g.

Finally we put back the detector on the second beam focus and started acquiring images with our nanowire THz imaging setup. We first acquired an image of the usual

USAF target to verify the image resolution. As shown in figure 4.5 the result was comparable with the result obtained using the pyroelectric sensor (here, actually, we had a little bit higher resolution because of a better beam focusing and arrived to solve completely the elements belonging to group 1 element 6, corresponding to a resolution of about $140\mu m$).

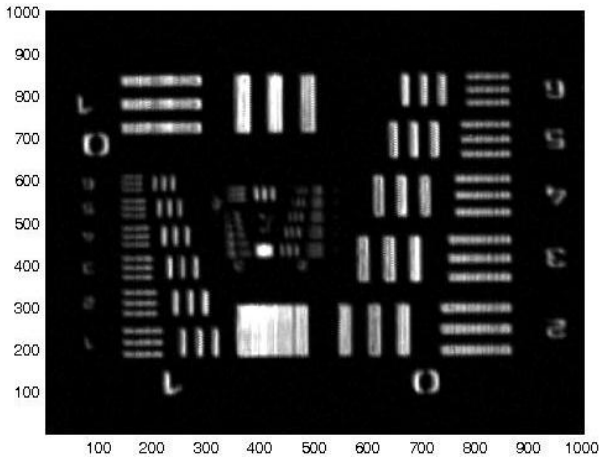

Figure 4.5: USAF target THz image using nanowire detector.

Good results were obtained using a dry leaf as a sample, acquired with the usual pixel pitch of about $100\mu m \times 100\mu m$, (figure 4.6).

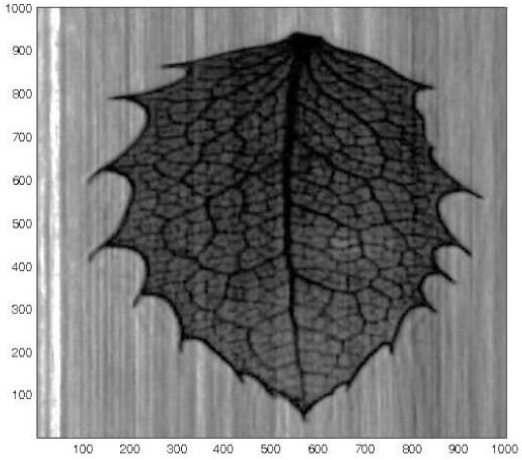

Figure 4.6: Dry leaf THz image using nanowire detector.

The striped background clearly observable in both images is due to the instability of nanowire response on long times (of the order of 5% in $10S$), an effect that is still under investigation.

4.2.2 Toward Terahertz digital holography

Terahertz Digital Holography is still an almost unexplored research field. Few results, in fact, have been obtained in this direction. The first experiment on Far IR DH dates back to 2006 when an off-axis transmission digital holography setup at millimetre wavelenghts was realized using a $100GHz$ Gun diode oscillator as a source and a spatially scanned Schottky diode as detector [34]. In 2008 computer simulations and an experimental realization of THz transmission digital holograms were realized with a THz TD technique [63]. Further transmission holography configurations were realized in 2011 using a $50mW$ far infrared gas laser at $2.52THZ$ and a pyroelectric camera [12] and using a frequency tunable continuous wave THz source emitting at $0.7THz$ and a spatially scanned schottky diode detector [23]. To date, however, no speckle holographic configuration has ever been realized and QCL THZ sources have never been used to this purpose. Our next step is to develop such a configuration using our QCL and a microbolometric camera: considered the low output power of our laser, a high sensitivity array is needed and therefore we decided to buy a focal plane array microbolometric camera, IRXCAM INO160THz [4;35]; this camera is composed of 160×120 VaO square pixels with $52\mu m$ pixel pitch and is optimized for the THz region detection in order to reach a NEP of $100pW$.

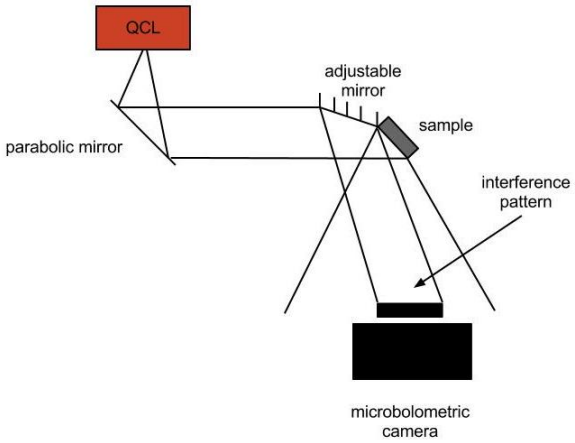

Figure 4.5: Simple THz holographic setup.

Our starting point will be the investigation of small scattering objects with a very simple and power saving configuration like the one illustrated in figure 4.5; in this configuration the laser beam is collimated by an OAP mirror and then it is intercepted both by the small object under investigation and by an adjustable mirror; the portion of the beam impinging on the sample, constitutes, as usual, the object beam while the portion of the beam reflected by the mirror constitutes the reference beam. With this configuration it is possible to obtain the desired fringe spacing simply changing the distance between the microbolometric camera and the sample and adjusting the mirror inclination. This simple configuration will be used to demonstrate the feasibility of the techniques but in a second step we will try to translate all the configurations developed in the field of Mid IR DH to the THz domain in order to take full advantage of the stability and of the increased field of view offered by a THz radiation DH setup.

5 Conclusions

During this PhD course I improved significantly my laboratory expertise since I had to face various arguments in the laser optics and imaging field. I had the opportunity to work on well-known lasers sources (CO_2 lasers) and detectors (pyroelectric cameras and detectors, microbolometric cameras) as well as on frontier sources (Quantum Cascade lasers) and innovative detectors (nanowires). I learnt to exploit the different characteristics of these specific coherent radiation sources and sensors to implement new and promising imaging techniques.

Nowadays we are witnessing a continuously growing interest in the Mid IR region and, even more, in the Far IR region, especially for imaging applications. Mid IR imaging systems are widely employed in the military and security field but also for energy saving and medical investigations and are, consequently, in continuous development. Even greater expectation is placed on imaging techniques in the Terahertz region, because of its well-known capacity to pass undisturbed through many common materials and to provide spectroscopic information about various strategic materials like explosives or drugs. In this scenario DH, a quite recent and peculiar imaging technique, is proving to be mature enough to play a key role among the numerous imaging techniques both in the thermal IR and in the Terahertz IR, especially for some specific applications. As we have seen, IRDH at $10.6\mu m$ has paved the way to large size object investigation, especially for non-destructive testing and, thanks to its ability to see through smoke, dust particles and flames, it could be employed, in the future, in military and safety applications. Mid IRDH could play a very important role also in the research activity about 3D display: holographic television, commonly regarded as the holy grail of holography, is one of the most promising and challenging developments for the future display market; only holography can provide all depth information necessary to obtain the reconstruction of natural-looking 3D scenes; IRDH, thanks to its capacity to record whole wavefront information of large size samples in daylight and not isolated conditions, and thanks

to the possible developments introduced by the progresses of spatial light modulators, may have an important role in this challenge. A desirable step to increase Mid IRDH could be accomplished if more compact sources, like QCLs, should replace the incredibly versatile but equally bulky CO_2 lasers; one of our future purposes is to pursue this result and to repeat all the successful experiments carried out in the Mid IR range in a miniaturized, and therefore more appealing and usable, version. All the results obtained in the Mid IR DH activity could be directly extended to the THz domain with improved results: an even lower vibration sensitivity and larger field of view should be obtained using a 10 times longer wavelenght than the one we have used up to now; further, the repeatedly highlighted capability of THz radiation to penetrate many materials impenetrable to visible light, combined with the capacity of DH to reconstruct the 3D images, would represent an invaluable tool to analyse internal structure with 3D perspective, otherwise not achievable. All these applications will receive an important impulse from the development on new and more sensitive and fast IR detectors like, hopefully, the nanowires FET tested with our imaging THz setup.

List of Publications

- M. Locatelli, E. Pugliese, M. Paturzo, V. Bianco, A. Finizio, A. Pelagotti**,** P. Poggi, L. Miccio, R. Meucci, and P. Ferraro, *Imaging alive people through smoke and flames by digital holography at far infrared*, to be published in Optics Express.
- E. Stoykova, F. Yaraş, H. Kang, L. Onural, A. Geltrude, M. Locatelli, M. Paturzo, A. Pelagotti, R. Meucci, P. Ferraro, *Visible reconstruction by a circular holographic display from digital holograms recorded under infrared illumination,* Optics Letters, Vol. 37, issue 15, pp. 3120-3122 (2012), Optical Society of America, DOI 10.1364/OL.37.003120.
- A. Pelagotti, M. Paturzo, M. Locatelli, A. Geltrude, R. Meucci, A. Finizio, P. Ferraro, *An automatic method for assembling a large synthetic aperture digital hologram,* Optics Express, Vol. 20, issue 5, pp. 4830-4839 (2012), Optical Society of America, DOI 10.1364/OE.20.004830.
- A. Pelagotti, M. Paturzo, A. Geltrude, M. Locatelli, R. Meucci, P. Poggi, P. Ferraro, *Digital holography for 3D imaging and display in the IR range: challenges and opportunities,* 3D Research, vol. 1, n. 4/06, pp. 1-10, Springer, ISSN: 2092-6731, DOI 10.1007/3DRes.04(2010)06.
- A. Pelagotti, M. Locatelli, A. Geltrude, P. Poggi, R. Meucci, M. Paturzo, L. Miccio, P. Ferraro, *Reliability of 3D Imaging by Digital Holography at Long IR Wavelength,* Journal of Display Technology, vol. 6, n. 10, pp. 465-471, OCTOBER 2010, Optical Society of America, ISSN: 1551-319X, DOI 10.1109/JDT.2010.2041186.
- M. Paturzo, A. Pelagotti, A. Finizio, L. Miccio, M. Locatelli, A. Geltrude, P. Poggi, R. Meucci, P. Ferraro, *Optical reconstruction of digital holograms recorded at 10.6 μm: route for 3D imaging at long infrared wavelengths,* Optics Letters, vol. 35, n. 12, pp. 2112-2114, June 15, 2010, Optical Society of America, ISSN: 0146-9592, DOI 10.1364/OL.35.002112.

Bibliography

[1] Allaria E., Brugioni S., De Nicola S., Ferraro P., Grilli S., Meucci R., *Digital holography at 10.6 μm,* Optics Communications 215, pp. 257-262 (2003).

[2] Bismuto A., Riedi S., Hinkov B., Beck M. Faist J., *Sb-free quantum cascade lasers in the 3–4 μm spectral range*, Semiconductor. Science and Technology 27, 045013 (2012).

[3] Blaser S., Yarekha D. A., Hvozdara L., Bonetti Y., Muller A., Giovannini M., Faist J., *Room-temperature, continuous-wave, single-mode quantum-cascade lasers at λ≃5.4 μm*, Applied Physics Letters, 86, 041109 (2005).

[4] Bolduc M., Terroux M., Tremblay B., Marchese L., Savard E., Doucet M., Oulachgar H., Alain C., Jerominek H., Bergeron A., *Noise-equivalent power characterization of an uncooled microbolometer-based THz imaging camera*, Proc. SPIE 80230C (2011).

[5] Born M., Wolf E., *Principles of optics, Electromagnetic theory of propagation, interference and diffraction of light*, [7ª ed. (expanse)], Cambridge University Press (1999).

[6] Cathabard O., Teissies R., Devenson J., Baranov A. N., *The 10th International Conference on Intersubband Transitions in Quantum Wells* (ITQW 2009) (National Research Council, Montreal, Canada, 2009), p.62.

[7] Chen Q., Jiang Z., Xu G. X., Zhang X. C., *Near-field terahertz imaging with a dynamic aperture*, Optics Letters, vol. 25, issue 15, 1122-1124 (2000).

[8] Chen H.T., Kersting R., Cho G., C., *Terahertz imaging with nanometer resolution*, Applied Physics Letters, vol. 83, n. 15, (2003).

[9] Cho A. Y. (ed.), *Molecular Beam Epitaxy*, AIP press, Woodbury, NY, (1997).

[10] Colombelli R., Capasso F., Gmachl C., Hutchinson A. L., Sivco D. L., Tredicucci A., Wanke M. C., Sergent A. M., Cho A. Y., Far-infrared surface-plasmon quantum-cascade lasers at 21.5 μm and 24 μm wavelengths, Applied Physics Letters, vol. 78, Issue 18 (2001).

[11] De Nicola S., Ferraro P., Grilli S., Miccio L., Meucci R., Buah-Bassuah P. K., Arecchi F. T., *Infrared digital reflective holographic 3D shape measurements*, Optics Communications 281, pp. 1445-1449 (2008).

[12] Ding S. H., Li Q., Li Y. D., Wang Q., *Continuous-wave terahertz digital holography by use of a pyroelectric array camera*, Optics Letters, Vol. 36, Issue 11, pp. 1993-1995, (2011).

[13] Dyakonov M., Shur M. S., *Shallow water analogy for a ballistic field effect transistor: New mechanism of plasma wave generation by dc current*, Physical Review Letters, vol. 71, issue 15, 2465-2468 (1993).

[14] Evans A., Nguyen J., Slivken S., Yu J. S., Darvish S. R., Razeghi M., *Quantum-cascade lasers operating in continuous-wave mode above 90 °C at λ ~ 5.25 μm*, Applied Physics Letters, 88, 051105 (2006).

[15] Faist J., Capasso F., Sivco D. L., Sirtori C., Hutchinson A. L., and Cho A. Y., *Quantum Cascade Laser*, Science 264, 553-556 (1994).

[16] Ferraro P., De Nicola S., Finizio A., Pierattini G., Coppola G., *Recovering image resolution in reconstructing digital off-axis holograms by Fresnel-transform method*, Applied Physics Letters, vol.85, n. 14, pp. 2709-2711, (2004)

[17] Ferraro P., Grilli S., Alfieri D., De Nicola S., Finizio A., Pierattini G., Javidi B., Coppola G., Striano V., *Extended focused image in microscopy by digital Holography*, Optics Express 13(18), 6738–6749 (2005)

[18] Gabor D., *A new microscopic principle*, Nature, 161, pp. 777–778 (1948).

[19] Geltrude A., Locatelli M., Poggi P., Pelagotti A., Paturzo M., Ferraro P., Meucci R., *Infrared digital holography for large object investigation* Proc. SPIE 8082-12, (2011).

[20] Georges M. P., Vandenrijt J. F., Stockman Y., Queeckers P., Dubois F., Doyle D., *Digital holographic interferometry with CO_2 lasers and diffuse illumination applied to large space reflector metrology*, Applied Optics Vol.52, No. 1, pp. A102-A116 (2012).

[21] Goodman J. W., *Introduction to Fourier Optics,* [2ª ed.], McGraw-Hill (1996).

[22] Goodman J. W., Lawrence R. W., *Digital image formation from electronically detected holograms*, Applied Physics Letters 11, pp. 77–79 (1967).

[23] Heimbeck M. S., Kim M. K., Gregory D. A., Everitt H. O., *Terahertz digital holography using angular spectrum and dual wavelength reconstruction methods*, Optics Express, Vol. 19, issue 10, pp. 9192-9200 (2011).

[24] Hu B. B., Nuss M. C. *Imaging with terahertz waves Optics Letters* **20** 1716–19 (1995).

[25] Kazarinov R. F., Suris R. A., *Possibility of amplification of electromagnetic waves in a semiconductor with a superlattice*, Sov. Phys. Semicond. 5, 707 (1971).

[26] Kohler R., Tredicucci A., Beltram F., Beere H. E., Linfield E. H., Davies A. G., Ritchie D. A., Iotti R. C., Rossi F., *Terahertz semiconductor heterostructure laser*, Nature 417, 156 (2002).

[27] Kreis T. M., Adams M., Jüptner W. P. O., *Methods of Digital Holography: A Comparison,* Proc. SPIE vol. 3098, 224-233 (1997).

[28] Kreis T. M., Jüptner W. P. O., *Principles of Digital Holography,* Proc. Of Fringe 97, Akademie Verlag Series in Optical Metrology vol. 3, 353-363 (1997).

[29] Lang S. B., Pyroelectricity: From Ancient Curiosity to Modern Imaging Tool, Physics Today, Volume 58, issue 8 (2005).

[30] Lee A. W., Williams B.S., Kumar S., Qing Hu, Reno J. L., *Real-time imaging using a 4.3-THz quantum cascade laser and a 320×240 element focal-plane array*, Photonics Technology Letters, IEEE

[31] Leith E. N., Upatnieks J., *Reconstructed wavefronts and communication theory,* Journal of the Optical Society of America, 52, pp. 1123-1130 (1962).

[32] Locatelli M., Pugliese E., Paturzo M., Bianco V., Finzizio A., Pelagotti A., Poggi P., Miccio L., Meucci R., Ferraro P., *Imaging alive people through smoke and flames by digital holography at far infrared*, to be published in Optics Express.

[33] Maes F., Vandermeulen D., Suetens P., *Medical image registration using mutual information*, Proc IEEE 91(10), 1699–1722 (2003).

[34] Mahon R. J., Murphy J. A., Lanigan W., *Digital holography at millimetre wavelengths*, Optics Communications, vol. 260, issue 2, 469–473 (2006).

[35] Marchese L., Bolduc M., Tremblay B., Doucet M., Oulachgar H., Le Noc L., Williamson F., Alain C., Jerominek H., Bergeron A., *A microbolometer-based THz imager*, Proc. SPIE 76710Z (2010).

[36] Meier R. W., *Magnification and Third-Order Aberrations in Holography*, Journal of the Optical Society of America vol. 55, n. 8, 987-992 (1965).

[37] Mittleman D. M., Hunsche S., Boivin L. Nuss M. C., *T-ray tomography*, Optics Letters, vol. 22, issue 22, pp. 904–906 (1997).

[38] Mittleman D. M., Jacobsen R. H., Nuss M. C., *T-ray imaging IEEE Sel. Top. Quantum Electron.* **2** 679–692 (1996).

[39] Onural L., Yaraş F., Kang H., *Digital Holographic Three-Dimensional Video Displays*, Proc. IEEE 99, 576 (2011).

[40] Patel C. K. N., *Continuous-Wave Laser Action on Vibrational-Rotational Transitions of CO2*, Physical Review 136 (5A), A1187–A1193 (1964).

[41] Paturzo M., Memmolo P., Finizio A., Näsänen R., Naughton T. J., Ferraro P., *Synthesis and display of dynamic holographic 3D scenes with real-world objects,* Optics Express 18, 8806-8815 (2010).

[42] Paturzo M., Pelagotti A., Finizio A., Miccio L., Locatelli M., Geltrude A., Poggi P., Meucci R., Ferraro P., *Optical reconstruction of digital holograms recorded at 10.6 μm: route for 3D imaging at long infrared wavelengths,* Optics Letters, vol. 35, n. 12, pp. 2112-2114, (2010).

[43] Pelagotti A., Locatelli M., Geltrude A., Poggi P., Meucci R., Paturzo M., Miccio L., Ferraro P., *Reliability of 3D Imaging by Digital Holography at Long IR Wavelength,* Journal of Display Technology, vol. 6, n. 10, pp. 465-471 (2010).

[44] Pelagotti A., Paturzo M., Geltrude A., Locatelli M., Meucci R., Poggi P., Ferraro P., *Digital holography for 3D imaging and display in the IR range: challenges and opportunities,* 3D Research, vol. 1, n. 4/06, pp. 1-10 (2010).

[45] Pelagotti A., Paturzo M., Locatelli M., Geltrude A., Meucci R., Finizio A., Ferraro P., *An automatic method for assembling a large synthetic aperture digital hologram,* Optics Express, Vol. 20, issue 5, pp. 4830-4839 (2012).

[46] Richards, P. L., Bolometers for infrared and millimeter waves, Journal of Applied Physics, Volume 76, issue 1, pp.1-24 (1994).

[47] Schnars U., Jüptner W. P. O., *Digital Holography, Digital Hologram Recording, Numerical Reconstruction and Related Techniques*, [1ª ed.], Springer (2005).

[48] Schnars U., Jüptner W. P. O., *Direct recording of holograms by a CCD target and numerical reconstruction*, Applied Optics, Vol. 33, No 2, pp. 179–181 (1994).

[49] Stadelmaier A., Massig J. H., *Compensation of lens aberrations in digital holography*, Optics Letters, vol. 25, issue 22, pp. 1630-1632 (2000).

[50] Stoykova E., Yaraş F., Kang H., Onural L., Geltrude A., Locatelli M., Paturzo M., Pelagotti A., Meucci R., Ferraro P., *Visible reconstruction by a circular holographic display from digital holograms recorded under infrared illumination,* Optics Letters, Vol. 37, issue 15, pp. 3120-3122 (2012).

[51] Suzuki S., Asada M., Teranishi A., Sugiyama H., Yokoyama H., *Fundamental oscillation of resonant tunneling diodes above 1 THz at room temperature*, Applied Physics Letters, Volume 97, issue 24 (2010)

[52] Tuft V. L., *Fringe resolution in digital holographic interferometry*, Department of Physics Norwegian University of Science and Technology Trondheim, Norway (2001).

[53] Vitiello M. S., Coquillat D., Viti L., Ercolani D., Teppe F., Pitanti A., Beltram F., Sorba L., Knap W., Tredicucci A., *Room-Temperature Terahertz detectors based on semiconductor nanowire field-effect transistors*, Nano Letters, vol. 12, issue 1, pp. 96-101 (2012).

[54] Vitiello M. S., Scamarcio G., Spagnolo V., Dhillon S. S.,Sirtori C., *Terahertz quantum cascade lasers with large wall-plug efficiency*, Applied Physics Letters, vol. 90, issue 19, 191115 (2007)

[55] Vitiello M. S., Viti L., Romeo L., Ercolani D., Scalari G., Faist J., Beltram F., Sorba L., Tredicucci, A., *Semiconductor nanowires for highly sensitive, room-temperature detection of terahertz quantum cascade laser emission*, Applied physics letters, vol. 100, issue 24, 241101 (2012)

[56] Walther C., Fischer M., Scalari G., Terazzi R., Hoyler N., Faist J., *Quantum cascade lasers operating from 1.2 to 1.6 THz*, Applied Physics Letters, 91, 131122 (2007).

[57] Wang S., Zhang X. C., *Tomographic imaging with a terahertz binary lens Applied Physics Letters* 82, 1821–1823 (2003).

[58] Williams B. S., Kumar S., Hu Q., Reno J. L., *High-power terahertz quantum cascade lasers*, Electron. Lett. 42, 89–91 (2006).

[59] Yang J., Ruan S., Zhang M., *Real-time continuous-wave terahertz imaging by a pyroelectric camera*, Chinese Optics Letters, vol. 6, n. 1, (2008).

[60] Yaraş F., *Three-dimensional holographic video display systems using multiple spatial light modulators*, Ph.D. dissertation (Bilkent University, 2011).

[61] Yaraş F., Kang H., Onural L., *Circular holographic video display System*, Optics Express vol. 19, n. 10, 9147-9156 (2011).

[62] Yaraş F., Kang H., Onural L., *State of the Art in Holographic Displays: A Survey*, Journal of Display Technology, 6, 10, 443-454 (2010).

[63] Zhang Y., Zhou W., Wang X., Cui Y., Sun W., *Terahertz Digital Holography*, Strain 44(5), 380–385 (2008).